INTERNATIONAL JOURNAL FOR NUMERICAL METHODS IN FLUIDS, VOL. 12, 407–441 (1991)

A GLOBALLY WELL-POSED FINITE ELEMENT ALGORITHM FOR AERODYNAMICS APPLICATIONS

G. S. IANNELLI AND A. J. BAKER

Department of Engineering Science and Mechanics, The University of Tennessee, Knoxville, TN 37996-2030, U.S.A.

SUMMARY

A finite element CFD algorithm is developed for Euler and Navier–Stokes aerodynamic applications. For the linear basis, the resultant approximation is at least second-order-accurate in time and space for synergistic use of three procedures: (1) a Taylor weak statement, which provides for derivation of companion conservation law systems with embedded dispersion-error control mechanisms; (2) a stiffly stable second-order-accurate implicit Rosenbrock–Runge–Kutta temporal algorithm; and (3) a matrix tensor product factorization that permits efficient numerical linear algebra handling of the terminal large-matrix statement. Thorough analyses are presented regarding well-posed boundary conditions for inviscid and viscous flow specifications. Numerical solutions are generated and compared for critical evaluation of quasi-one- and two-dimensional Euler and Navier–Stokes benchmark test problems. Of critical importance, essentially non-oscillatory solutions are uniformly attained for a range of supercritical flow situations with shocks.

KEY WORDS Compressible Navier–Stokes equations Taylor weak statement Curvilinear co-ordinate dissipation Lyapunov stability theory Well-posed boundary conditions Finite element semi-discretization Implicit Rosenbrock–Runge–Kutta scheme Tensor matrix product factorization

1. INTRODUCTION

This paper documents the derivation and performance verification of an implicit and stiffly stable Galerkin finite element algorithm for the compressible Navier–Stokes equations that is semi-discretely stable and second-order-accurate on arbitrary meshes. The theoretical developments then lead to a terminal fully discrete algebraic system that is efficiently solved non-iteratively for large Courant numbers.

The need to meet these fundamental requirements, namely stability, accuracy and efficiency for arbitrary meshes in a single practical scheme, has motivated the development of a variety of significant algorithms in the last two decades. A notable contribution was published by Beam and Warming,[1] who proposed a central difference implicit factored scheme for the Euler equations, wherein the unknown state variable constitutes the solution of an efficient sequence of block-tridiagonal linear systems. This procedure forms the basis of the ARC-2D, ARC-3D code family that has allowed investigation of a wide range of transonic and supersonic flows. However, as confirmed by Pulliam,[2] the basic scheme must be augmented by a blend of second- and fourth-order dissipative difference expressions to maintain stability in the presence of shocks. This leads to a block-pentadiagonal matrix system if the full Jacobian matrix of the necessary artificial dissipation is included in the implicit formulation. The original matrix structure can be maintained by using only explicit fourth-order damping, which limits the magnitude of stable time steps. The associated Courant number may not be much larger than unity for accurate unsteady simulations, since the time integrator is the intrinsically non-dissipative Crank–Nicolson rule.

0271–2091/91/050407–35$17.50

Received 12 May 1989
Revised 20 March 1990

In parallel with space-centred schemes, upwind methods have been developed to dispense with the explicit addition of numerical dissipation. Notable procedures evolving flux vector and flux difference splittings include those of Steger and Warming,[3] van Leer[4] and Roe,[5] wherein the upwind differencing is performed in directions opposite to the characteristic directions and thereby inherently introduces an amount of artificial dissipation. These algorithms have been implemented both explicitly and implicitly[4] and have generated crisp non-oscillatory shocks for quasi-1D gasdynamics flows. Recently, Liou and van Leer[6] have presented a thorough comparison of various splittings and conclude that a robust algorithm is achieved by using different splittings for the implicit and explicit operators. The geometric appeal of these constructions is considerable, since the derivations pivot on classical notions of characteristics, hence signal propagation directions. However, the straightforward extension of these intrinsically 1D schemes to multi-dimensional formulations leads to formulational ambiguities, hence algorithms that are extensively coupled to the underlying grid. Powell and van Leer[7] have addressed this crucial issue and developed a 'cell vertex scheme where the grid components of the convection speed are known'. This entails local decomposition of the Euler equations into a set of convection equations so that conservation of mass, momentum and energy is satisfied. Therefore the resulting scheme is algebraically rather involved and their results remain affected by a usually modest dispersion error.

An alternative formulation is proposed by Lerat,[8] who develops a fully discrete space-centred finite difference scheme for the Euler equations that, importantly, introduces an inherent coupling of the time derivatives of the unknown variable at various adjacent nodes. This feature distinguishes this scheme from Beam and Warming's and intrinsically introduces an adequate amount of dissipation without added fourth-order difference expressions. This mechanism produces an algorithm that remains stable in the presence of shocks. The original development is based on uniform mesh and time step increments and leads to a variety of algorithms upon selection of specific numerical values for imbedded parameters.

The notion of time derivative coupling is natural in the finite element method, via the semi-discretization mass matrix, and leads to schemes that are not affected by odd–even node decoupling for dissipative spatial semi-discretizations devoid of fourth-order difference terms. In this framework, Fletcher[9] proposed a group-approximation least-squares algorithm for subsonic flows, while Tezduyar and Hughes[10] developed Petrov–Galerkin schemes to introduce adequate dissipation in a weak statement formulation. In distinction to these developments, Donea[11] derived the 'Taylor–Galerkin' finite element algorithm for hyperbolic equations. This formulational procedure employs a truncated Taylor series to generate a time-semi-discrete conservation law system which is subsequently discretized in space with bilinear basis functions. In this instance several stability mechanisms are introduced in continuous form upon restatement of the time derivatives with spatial derivatives via the original conservation law system.

This fundamental procedure has been thoroughly analysed by Baker and Kim,[12] who develop the 'Taylor weak statement' generalization for hyperbolic conservation law systems. This construction develops a so-called companion conservation law system that contains continuum expressions representing intrinsic dissipation terms. Whereupon, the standard Galerkin finite element fully discrete algorithm yields over a dozen independently derived schemes upon identification of the imbedded parameter set. The analysis indicates that the companion conservation law system approach can lead to stable centred semi-discrete schemes on arbitrary grids upon selection of opportune length and velocity scales in the continuum dissipation operator.

A significant advancement in the area of stable boundary conditions for the full compressible Navier–Stokes equations was presented by Dutt,[13] who derived statements for 'maximally dissipative' boundary conditions. In his analysis these are determined such that the time variation

of a Navier–Stokes system energy functional is bounded. The development focused on essentially unidirectional flows and heuristically assumes that a bounded energy time variation induces a bounded solution.

Herein, Dutt's analysis is generalized for multidimensional problems and is interpreted as an application of a generalized Lyapunov stability theory.[14–16] Stable boundary conditions for the Navier–Stokes equations are derived and their dependence on inflow and outflow Mach number is clearly identified and assessed. Further, the connection between bounded energy variation and a stable solution is analytically established. The derived conditions constrain the outflow static pressure and the surface deviatoric tractions, as well as momentum and heat fluxes, and can be effectively enforced via the Galerkin-weak-statement-derived surface integrals.

The Taylor weak statement is the basis for the development of the present Galerkin algorithm that employs a second-order non-linear dissipation operator. The latter is valid on arbitrary meshes upon selection of the computational space contravariant velocity components, multiplied by the determinant of the co-ordinate transformation Jacobians, as the representative scales. Of significance, the developed stability correction is sufficient to allow crisp and monotone solutions for large Courant number in the framework of an implicit block-tridiagonal linear algebra solver. This is attained via combination of this stability mechanism with a finite element double interpolation, to reduce local truncation error in the flux vector semi-discretization, and an implicit Rosenbrock–Runge–Kutta time integration, to simultaneously obtain second-order accuracy and stiff stability. The terminal sparse matrix system is then efficiently solved via a tensor product factorization. The developed finite element CFD algorithm is verified for a range of transonic aerodynamic flows. These include a quasi-1D shocked flow in an off-design de Laval nozzle, and 2D inviscid and viscous laminar flows about a parabolic arc aerofoil. All CFD solutions are verified monotone throughout the computational domain, including the boundaries, and each accurately resolves all flow features, including shocks and shock-induced massive boundary layer separation.

The outline of this paper is as follows. Section 2 presents the appropriate conservation law form and attendant non-dimensionalization, and Section 3 details the derivation of the selected conservation law system and formulation of the continuum weak statement. In Section 4, well-posed boundary conditions are derived using a recently proved Lyapunov stability theorem, whereupon pertinent implementation issues are discussed. Subsequently, a method for initial condition generation is derived in Section 5. The finite element spatial semi-discretization is developed in Section 6 and the implicit Rosenbrock–Runge–Kutta scheme is presented in Section 7. To conclude, Section 8 details the tensor product factorization and Section 9 presents the results for the selected benchmark numerical validations.

2. CONSERVATION LAW SYSTEM

The partial differential equation system governing compressible viscous flows written in conservation law form is

$$\mathscr{L}(q)=\frac{\partial q}{\partial t}+\nabla\cdot(\mathbf{f}-\mathbf{f}^{v})=0 \quad \text{on } \mathbb{R}^{+}\times\Omega,\ \Omega\subset\mathbb{R}^{n}, \tag{1}$$

where $\mathbb{R}^{+}$ denotes the positive real number field and n denotes the spatial dimensionality. Further, $q=q(\mathbf{x}, t)$ is the state variable $\mathbf{f}=\mathbf{f}(q)$ is the kinematic–kinetic flux vector and $\mathbf{f}^{v}=\mathbf{f}^{v}(q)$ contains the constitutive dissipation fluxes. In the sequel a lowercase letter denotes an array, a capital letter denotes a square matrix and boldface signifies a vector.

The Cartesian component Navier–Stokes equations are obtained for (1), using subscript i, j tensor indices, through the following specifications:

$$q \equiv \begin{Bmatrix} \rho \\ m_i \\ e \end{Bmatrix}, \qquad \mathbf{f} \Rightarrow f_j = \begin{Bmatrix} m_j \\ m_i m_j/\rho + p\delta_{ij} \\ (e+p)m_j/\rho \end{Bmatrix}, \tag{2}$$

$$\mathbf{f}^v \Rightarrow f_j^v = \begin{Bmatrix} 0 \\ \sigma_{ij} \\ \sigma_{ij} m_i/\rho + [\gamma/RePr(\gamma-1)]\partial T/\partial x_j \end{Bmatrix}. \tag{3}$$

The non-dimensional deviatoric stress tensor σ_{ij} is defined as

$$\sigma_{ij} = \frac{1}{Re}\left\{\frac{\partial(m_i/\rho)}{\partial x_j} + \frac{\partial(m_j/\rho)}{\partial x_i} - \frac{2}{3}\frac{\partial(m_k/\rho)}{\partial x_k}\delta_{ij}\right\}. \tag{4}$$

In expressions (2)–(4), ρ is the fluid density, $m_i = \rho u_i$ is the linear momentum, e is the total specific energy and p is the static pressure, which is assumed to satisfy the polytropic gas law

$$p = (\gamma-1)\left(e - \frac{m_i m_i}{2\rho}\right), \tag{5}$$

where γ is the specific heat ratio.

The typical reference state for the non-dimensionalization of $q(\mathbf{x}, t)$ and the flux vectors $\mathbf{f}$ and $\mathbf{f}^v$ is the inlet state, with density ρ_∞ and principal velocity component U_∞, as well as a convenient length measure L. Time is scaled by L/U_∞ whereas static pressure and total specific energy e are scaled by the reference dynamic pressure $\rho_\infty U_\infty^2$. Hence the static temperature non-dimensionalization is via U_∞^2/R, where R is the polytropic gas constant, yielding the reference temperature

$$T_{\text{ref}} = \frac{U_\infty^2}{R} = \gamma\left(\frac{U_\infty^2}{\gamma R T_\infty}\right) T_\infty = \gamma M_\infty^2 T_\infty, \tag{6}$$

where M_∞ is the freestream Mach number and T_∞ is the corresponding temperature. Consequently, the non-dimensional static temperature definition is

$$T = \frac{\gamma-1}{\rho}\left(e - \frac{m_i m_i}{2\rho}\right). \tag{7}$$

Finally, Re and Pr denote the Reynolds and Prandtl numbers respectively, defined as

$$Re \equiv \frac{\rho_\infty U_\infty L}{\mu_\infty}, \qquad Pr = \frac{c_p \mu_\infty}{k_\infty}, \tag{8}$$

where c_p is the specific heat at constant pressure while μ_∞ and k_∞ are the freestream dynamic viscosity and heat conductivity respectively. In the sequel the term $\gamma/RePr(\gamma-1)$ is indicated by $(Pe)^{-1}$, the inverse of a generalized Peclet number. Note that with this non-dimensionalization the Mach number M_∞ does not explicitly appear in the governing equations. However, its influence is reflected in the magnitude of the inlet total specific energy e.

3. TAYLOR WEAK STATEMENT ALGORITHM

The dominant error mode introduced in the spatial semi-discretization of (1) is dispersive, which can propagate throughout the computational domain, hence corrupt the approximate solution process and possibly lead to iterative divergence. Furthermore, since **f** is a non-linear function of q, (1) admits non-smooth solutions containing shock waves, rarefactions and contact discontinuities which aggravate this intrinsic error mechanism. To counter such solution degradation, we derive a '*companion conservation law system*' such that its semi-discrete analogue solution closely models that of the given system (1). Then a stable and efficient time integration is achieved via a non-linearly stable implicit Rosenbrock–Runge–Kutta (IRK) algorithm.[17]

3.1. Companion conservation law system

The companion conservation law system is developed via augmentation of (1) with an expression identified through semi-discrete truncation error determination via the the corresponding TWS theory.[12] The developed modified conservation law system is amenable to exacting analysis for both dispersive and dissipative semi-discrete and/or fully discrete error mechanisms. A Taylor series identifies lead truncation error terms in a time semi-discretization of the inviscid Euler equation subset of (1). The analysis focuses on this system since a centred semi-discretization of the convection terms in **f**, thereto associated, is the operation that triggers emergence of dispersive instability. Thereupon, the second time derivative is re-expressed in terms of spatial derivatives of **f** of the original partial differential equations. The arbitrariness intrinsic to this procedure introduces parameters eligible for constraints, such that an optimally accurate and/or stable semi-discrete solution procedure can be generated by solving the resultant ordinary differential equation (ODE) system.

Assuming the solution of the Euler form of (1) exists, and is at least three times differentiable, a Taylor series exists of the form

$$q^n = q^{n+1} - \Delta t\left(\frac{\partial q}{\partial t}\right)^{n+1} + \frac{(\Delta t)^2}{2}\left(\frac{\partial^2 q}{\partial t^2}\right)^{n+1} - \frac{(\Delta t)^3}{6}\left(\frac{\partial^3 q}{\partial t^3}\right)^{n^+}, \tag{9}$$

where $\Delta t \equiv t^{n+1} - t^n$ with n denoting the discrete time index and n^+ indicating a time level between n and $n+1$. If the implicit backwards Euler rule is applied to (1) for $f_j^v = 0$, the resulting scheme is

$$\frac{q^{n+1} - q^n}{\Delta t} = -\nabla \cdot \mathbf{f}, \tag{10}$$

which is recast via (9) as

$$\frac{\partial q}{\partial t} + \nabla \cdot \mathbf{f} - \frac{\Delta t}{2}\left(\frac{\partial^2 q}{\partial t^2}\right) + \frac{\Delta t^2}{6}\left(\frac{\partial^3 q}{\partial t^3}\right)^{n^+} = 0. \tag{11}$$

The implicit Euler rule is known to introduce substantial artificial dissipation which, according to relation (11), is expressed by the second partial derivative in time of the state variable q. Therefore this derivative is selected as the basis for an effective numerical dissipation term that stabilizes central scheme semi-discrete convection terms.

The following derivations detail the modifications employed to synthesize a dissipation mechanism that allows second-order time accuracy, independent of Δt, which decreases in intensity as a representative length parameter is reduced. For the curvilinear co-ordinate Euler

equations the second time derivative in (11) may be expressed as

$$\left(\frac{\partial^2 q}{\partial t^2}\right)\Delta t = s = \frac{1}{\det J}\left[\frac{\partial}{\partial \eta_k}\left(e_{jk}\frac{\partial f_j}{\partial q}\frac{e_{il}}{\det J}\frac{\partial f_i}{\partial q}\Delta t\frac{\partial q}{\partial \eta_l}\right)\right]. \tag{12}$$

Here J denotes the co-ordinate transformation Jacobian matrix with entries $\partial x_j/\partial \eta_i$ and determinant $\det J$, and e_{ij} are the elements of the matrix $(\det J)J^{-1}$. In (12), Δt is replaced by the curvilinear co-ordinate Courant number expression

$$\Delta t = \frac{C_{\underline{i}}}{|a_{\eta_{\underline{i}}}|}\Delta \eta_{\underline{i}}, \tag{13}$$

where C_i is associated with a_{η_i}, the ith physical component of velocity in the curvilinear co-ordinate system $\boldsymbol{\eta}$. Using tensor analysis,[18] this component is expressible in 2D as

$$\alpha_{\eta_i} = \frac{1}{\det J}\,|e_{j\underline{i}}u_j|\,(e_{k(3-\underline{i})}e_{k(3-\underline{i})})^{1/2}. \tag{14}$$

Inserting this into (13) yields

$$\Delta t = \frac{C_{\underline{i}}}{|e_{j\underline{i}}u_j|\,(e_{k(3-\underline{i})}e_{k(3-\underline{i})})^{1/2}/\det J}\Delta \eta_{\underline{i}}, \tag{15}$$

whereupon the dissipation limiter β_i is defined as

$$\beta_{\underline{i}} \equiv \frac{C_{\underline{i}}}{(e_{k(3-\underline{i})}e_{k(3-\underline{i})})^{1/2}}. \tag{16}$$

Subsequently, inserting (15) and (16) into (12) yields

$$s = \frac{1}{\det J}\left[\frac{\partial}{\partial \eta_k}\left(e_{jk}\frac{\partial f_j}{\partial q}e_{il}\frac{\partial f_i}{\partial q}\frac{\beta_{\underline{i}}\Delta \eta_{\underline{i}}}{|e_{r\underline{i}}u_r|}\frac{\partial q}{\partial \eta_l}\right)\right]. \tag{17}$$

This expression is further simplified as follows. First, the indices k and l are contracted, whereupon the product $e_{jk}(\partial f_j/\partial q)e_{ik}(\partial f_i/\partial q)$ comprises the term $e_{jk}u_je_{ik}u_i$. Hence this suggests the replacement

$$\frac{e_{jk}\dfrac{\partial f_j}{\partial q}e_{ik}\dfrac{\partial f_i}{\partial q}}{|e_{r\underline{i}}u_r|} \Rightarrow D(e_{jk}u_je_{ik}u_i)^{1/2} \equiv D|\mathbf{u}|, \tag{18}$$

where D is a constant positive diagonal matrix. Consequently, the terminal simplified form of (17) is

$$s = \frac{\mathbf{B}}{\det J}\left[\frac{\partial}{\partial \eta_l}\left(|\mathbf{u}|\frac{\partial q}{\partial \eta_l}\right)\right], \tag{19}$$

where B (capital beta) is a diagonal matrix of at present arbitrary coefficients. Note that the magnitude of this form of dissipation vanishes as the values of the metrics e_{ik} in $|\mathbf{u}|$ decrease, as they do under grid refinement. The operator s is then explicitly added to (1) to yield the desired '*companion conservation law system*'

$$\frac{\partial q}{\partial t} + \frac{\partial}{\partial x_k}(f_k - f_k^v) - \frac{\mathbf{B}}{\det J}\frac{\partial}{\partial \eta_l}\left(|\mathbf{u}|\frac{\partial q}{\partial \eta_l}\right) = 0. \tag{20}$$

Thereupon, the convection terms in this system can be spatially semi-discretized using intrinsically non-dissipative centred schemes, i.e. a Galerkin method,[19] to yield a stable ODE system. Note that if this ODE system is stable for $Re \to \infty$, then it is all the more so when Re is finite, since centred scheme semi-discretizations of diffusion terms are intrinsically stable.

3.2. *Weak statement*

A weak statement for (20) is written as

$$\int_\Omega w\left[\frac{\partial q}{\partial t}+\frac{\partial}{\partial x_k}(f_k-f_k^v)-\frac{\mathbf{B}}{\det J}\frac{\partial}{\partial \eta_l}\left(|\mathbf{u}|\frac{\partial q}{\partial \eta_l}\right)\right]\mathrm{d}\Omega=0, \quad \forall w, \tag{21}$$

where w is a representative arbitrary element of the Hilbert space S^m for $m \geqslant 0$. The associated symmetrized weak statement form is developed by transforming (21) using a Green–Gauss theorem yielding

$$\int_\Omega w\frac{\partial q}{\partial t}\mathrm{d}\Omega-\int_\Omega \frac{\partial w}{\partial x_k}(f_k-f_k^v)\,\mathrm{d}\Omega+\mathbf{B}\int_{\Omega_\eta}|\mathbf{u}|\frac{\partial w}{\partial \eta_l}\frac{\partial q}{\partial \eta_l}\,\mathrm{d}\eta+\oint_{\partial\Omega} w f_j n_j\,\mathrm{d}\Gamma-\oint_{\partial\Omega} w f_j^v n_j\,\mathrm{d}\Gamma=0, \quad \forall w\in S^1, \tag{22}$$

where Ω_η is the image of Ω in η-space and n_j denotes the jth component of the outward-pointing unit vector $\mathbf{n}$ on the boundary $\mathrm{d}\Gamma$ of $\mathrm{d}\Omega$. This system is, by components of q,

$$\int_\Omega w\frac{\partial \rho}{\partial t}\,\mathrm{d}\Omega-\int_\Omega \frac{\partial w}{\partial x_k}m_k\,\mathrm{d}\Omega+\beta_\rho\int_{\Omega_\eta}|\mathbf{u}|\frac{\partial w}{\partial \eta_l}\frac{\partial \rho}{\partial \eta_l}\,\mathrm{d}\eta+\oint_{\partial\Omega} w m_j n_j\,\mathrm{d}\Gamma=0 \tag{23}$$

for the continuity equation,

$$\int_\Omega w\frac{\partial m_i}{\partial t}\,\mathrm{d}\Omega-\int_\Omega \frac{\partial w}{\partial x_k}\left(\frac{m_k}{\rho}m_i+p\delta_{ki}\right)\mathrm{d}\Omega+\int_\Omega \frac{\partial w}{\partial x_k}\sigma_{ik}\,\mathrm{d}\Omega+\beta_{m_i}\int_{\Omega_\eta}|\mathbf{u}|\frac{\partial w}{\partial \eta_l}\frac{\partial m_i}{\partial \eta_l}\,\mathrm{d}\eta$$
$$+\oint_{\partial\Omega} w p\delta_{ki}n_k\,\mathrm{d}\Gamma+\oint_{\partial\Omega} w\frac{m_i}{\rho}m_j n_j\,\mathrm{d}\Gamma-\oint_{\partial\Omega} w\sigma_{ij}n_j\,\mathrm{d}\Gamma=0 \tag{24}$$

for the momentum equations, $1 \leqslant i \leqslant n=2$, and

$$\int_\Omega w\frac{\partial e}{\partial t}\,\mathrm{d}\Omega-\int_\Omega \frac{\partial w}{\partial x_k}\left(\frac{m_k}{\rho}(e+p)\right)\mathrm{d}\Omega+\int_\Omega \frac{\partial w}{\partial x_k}\left(\frac{m_i}{\rho}\sigma_{ik}\right)\mathrm{d}\Omega+Pe^{-1}\int_\Omega \frac{\partial w}{\partial x_k}\frac{\partial T}{\partial x_k}\,\mathrm{d}\Omega$$
$$+\beta_e\int_{\Omega_\eta}|\mathbf{u}|\frac{\partial w}{\partial \eta_l}\frac{\partial e}{\partial \eta_l}\,\mathrm{d}\eta+\oint_{\partial\Omega} w(e+p)\frac{m_j}{\rho}n_j\,\mathrm{d}\Gamma-\oint_{\partial\Omega} w\frac{m_i}{\rho}\sigma_{ij}n_j\,\mathrm{d}\Gamma-Pe^{-1}\oint_{\partial\Omega} w\frac{\partial T}{\partial n}\,\mathrm{d}\Gamma=0 \tag{25}$$

for the energy equation.

Note that the momentum flux, deviatoric tractions and heat flux are the integrands of the respective flux vector term surface integrals. Their naturally occurring presence permits effective implicit imposition of all appropriate boundary conditions. Conversely, the surface integral resulting from the TWS-generated term may be discarded to provide the intrinsically weak homogeneous Neumann boundary condition for the dissipation operator term (19). This action guarantees well-posedness for the companion conservation law system (20) even as $Re \to \infty$.

4. BOUNDARY CONDITIONS

The numbers of Dirichlet boundary conditions for the n-dimensional Euler/Navier–Stokes equations that derive from Strikwerda's work[20] are as follows.

Navier–Stokes equations

$n+2$ conditions on an inflow boundary
$n+1$ conditions on an outflow boundary.

Euler equations

$n+2$ conditions for supersonic inflow
$n+1$ conditions for subsonic inflow
1 condition for subsonic outflow
0 conditions for supersonic outflow.

Here n is the dimension of Ω. An admissible specific boundary condition set can be derived following Dutt's analysis,[13] whereupon it is shown that the weak statement (12) provides by default the venue to enforce the derived well-posed conditions rigorously and efficiently.

4.1. *Choice of boundary conditions*

This analysis details the derivation of a specific set of boundary conditions that promotes solution boundedness for (1), hence (23)–(25). For an arbitrary partial differential equation system this can be established upon invoking Lyapunov stability theory.[14–16] This theory is based on a non-decreasing functional, or generalized system energy, and its total time derivative as associated with the given equation set. As shown in the sequel, the stability expression can be cast in terms of functions on the boundary Γ of the domain Ω, which can be constrained to satisfy the following generalized stability theorem, recently attained.

Theorem 1 (*Iannelli*)

Let $V=V(t, q)$ be a Lyapunov function defined on $\mathbb{R}^+ \times \mathbb{R}^n$, with $t \in \mathbb{R}^+$ and $q \in \mathbb{R}^n$, which satisfies the conditions:

(1) $c(\|q\|) \leqslant V(t, q)$, where $c(\|q\|)$ is a continuously increasing function and $c(\|q\|) \to \infty$ as $\|q\| \to \infty$
(2) $(\mathrm{d}V/\mathrm{d}t)_{\mathrm{PDE}} = f(t, q) - g(t, q)$, where subscript 'PDE' denotes a time derivative along a solution q of the given partial differential equation, f is a continuous function bounded above and g is a positive continuously increasing function.

Then the solutions q are bounded.

Proof. If $f(t, q) \leqslant 0$, then this theorem reverts to the classical Lyapunov theory stability condition proved in Reference 16. Conversely, if $f(t, q) > 0$, then the theorem is proved by contradiction:

(i) suppose $\exists\ t^* \backslash (\mathrm{d}V/\mathrm{d}t)_{\mathrm{PDE}} = f(t, q) - g(t, q) > 0,\ \forall t > t^*$
(ii) $\Rightarrow g(t, q) < f(t, q),\ \forall q(\mathbf{x}, t) \backslash t > t^*$
(iii) $\Rightarrow V(t, q)$ grows $\forall t > t^*$
(iv) $\Rightarrow \|q(\mathbf{x}, t)\|$ grows $\forall t > t^*$, since $V(t, q)$ is continuously increasing

(v) $\Rightarrow \exists\ \mathbf{x}_b,\ \tilde{t} \setminus g(t, q(\mathbf{x}, t)) > \max\{f(t, q(\mathbf{x}, t))\},\quad \forall t > \tilde{t}\ \ \forall \mathbf{x} \in S \equiv \{\mathbf{x} : \|\mathbf{x} - \mathbf{x}_b\| \leqslant \delta\} \subset \Omega,\ \ \delta > 0,$ since $g(t, q(\mathbf{x}, t))$ is continuously increasing and $\max\{f(t,\ q(\mathbf{x}, t))\} \leqslant K = \text{const.}$, since f is bounded.

However, (v) contradicts (ii), hence (i) does not hold $\forall t > t^*$, consequently $q(\mathbf{x}, t)$ does not grow $\forall t > \tilde{t}$. An analogous contradiction is reached by assuming in (i) an opposite inequality for the time derivative of V. Therefore, $q(\mathbf{x}, t)$ can be at most a bounded oscillatory function since $V(t, q)$ is analogous, though not equal, to a norm of $q(\mathbf{x}, t)$ and $V_{\min}(t, q) \leqslant V(t, q) \leqslant V_{\max}(t, q)$, with $V_{\max}(t, q) \leqslant K = \text{const.}$, since (i) does not hold $\forall t > t^*$. □

The application of this theorem can be exemplified via determination of the well-known admissible boundary condition for a linear hyperbolic partial differential equation. Thereafter, the corresponding boundary conditions for the full Navier–Stokes system are established. The linear model equation is

$$\frac{\partial q}{\partial t} + u\frac{\partial q}{\partial x} = 0, \tag{26}$$

defined in the domain $\Omega \equiv [a, b] \times [t_0, \infty)$, where u is a positive constant. The well-posed boundary condition for (26) is

$$q(a, t) = q_a(t), \tag{27}$$

which is readily derived as follows. An admissible Lyapunov functional associated to (26) is

$$V = \tfrac{1}{2}\int_a^b q^2\, \mathrm{d}x, \tag{28}$$

with time derivative

$$\frac{\mathrm{d}V}{\mathrm{d}t} = \int_a^b q\frac{\partial q}{\partial t}\mathrm{d}x. \tag{29}$$

Equation (29), upon substitution of $\partial q/\partial t$ via (26), becomes

$$\frac{\mathrm{d}V}{\mathrm{d}t} = -u\int_a^b q\frac{\partial q}{\partial t}\mathrm{d}x = -u\int_a^b \frac{\partial}{\partial x}\left[\frac{q^2}{2}\right]\mathrm{d}x, \tag{30}$$

which can be integrated exactly exposing the boundary function

$$\frac{\mathrm{d}V}{\mathrm{d}t} = u\left[\frac{q^2}{2}\right]_{x=a} - u\left[\frac{q^2}{2}\right]_{x=b}. \tag{31}$$

Note that (31) satisfies the hypotheses of Theorem 1 upon setting $q(a, t) = q_a(t)$, where $q_a(t)$ is a continuous function bounded above. Consequently, the boundary condition (27) is well posed.

Dutt's analysis indicates that a system energy functional for the full Navier–Stokes equations can be derived utilizing an 'entropy' functional of the Euler equations, which we select as

$$V(q) = \rho\left[\gamma\log\left(\frac{\rho}{\bar{\rho}}\right) - \log\left(\frac{p}{\bar{p}}\right) + \frac{(\gamma-1)\bar{\rho}m_i m_i}{2\bar{p}\rho^2} - \gamma + \frac{p\bar{\rho}}{\bar{p}\rho}\right] + (\gamma - 1)\bar{\rho}, \tag{32}$$

where $\bar{p}$ and $\bar{\rho}$, to be determined, represent a reference thermodynamic state such that

$$V(q) - (\gamma - 1)\bar{\rho} \geqslant 0 \tag{33}$$

and

$$\left(\frac{\bar{\rho}}{\bar{p}}-\frac{\rho}{p}\right)\leqslant 0. \tag{34}$$

It is shown in Reference 13 that V in (32) is a strictly positive and convex function that satisfies the relation

$$\frac{\partial V}{\partial q}\frac{\partial f_j}{\partial q}=\frac{\partial F_j}{\partial q}, \tag{35}$$

where the expressions for F_j and $\partial V/\partial q$ are

$$F_j=\frac{m_j}{\rho}[V(q)-(\gamma-1)\bar{\rho}], \tag{36}$$

$$\frac{\partial V}{\partial q}=\left\{\begin{array}{c}\gamma\log\left(\dfrac{\rho}{\bar{\rho}}\right)-\log\left(\dfrac{p}{\bar{p}}\right)-\dfrac{(\gamma-1)m_i m_i}{2\rho p}\\ \dfrac{m_i(\gamma-1)}{p}\\ (\gamma-1)\left(\dfrac{\bar{\rho}}{\bar{p}}-\dfrac{\rho}{p}\right)\end{array}\right\}^{\mathrm{T}}. \tag{37}$$

The Lyapunov functional is defined as

$$S(t)\equiv\int_{\Omega}V(q(\mathbf{x},t))\,\mathrm{d}\Omega, \tag{38}$$

where $\partial V/\partial t$ is derived utilizing the Navier–Stokes equations as follows. First

$$\frac{\partial V}{\partial q}\frac{\partial q}{\partial t}+\frac{\partial V}{\partial q}\frac{\partial f_j}{\partial x_j}-\frac{\partial V}{\partial q}\frac{\partial f_j^{\nu}}{\partial x_j}=0, \tag{39}$$

hence

$$\frac{\partial V}{\partial t}+\frac{\partial V}{\partial q}\frac{\partial f_j}{\partial q}\frac{\partial q}{\partial x_j}-\frac{\partial V}{\partial q}\frac{\partial f_j^{\nu}}{\partial x_j}=0, \tag{40}$$

whereupon, using (35),

$$\frac{\partial V}{\partial t}+\frac{\partial F_j}{\partial x_j}-\frac{\partial V}{\partial q}\frac{\partial f_j^{\nu}}{\partial x_j}=0. \tag{41}$$

Consequently, the Lyapunov functional time derivative is

$$\frac{\mathrm{d}S}{\mathrm{d}t}=-\int_{\Omega}\left(\frac{\partial F_j}{\partial x_j}-\frac{\partial V}{\partial q}\frac{\partial f_j^{\nu}}{\partial x_j}\right)\mathrm{d}\Omega. \tag{42}$$

Integrating (42) by the Green–Gauss theorem yields

$$\frac{\mathrm{d}S}{\mathrm{d}t}=-\oint_{\partial\Omega}\left(F_j n_j-\frac{\partial V}{\partial q}f_j^{\nu}n_j\right)\mathrm{d}\Gamma-\int_{\Omega}\frac{\partial V_q}{\partial x_j}f_j^{\nu}\,\mathrm{d}\Omega. \tag{43}$$

Since the domain integral in (43) is positive,[13] the following inequality is obtained for the time derivative of S:

$$\frac{dS}{dt} \leqslant -\oint_{\partial\Omega} \frac{\mathbf{m}}{\rho}\cdot\mathbf{n}[V(q)-(\gamma-1)\bar{\rho}]\,d\Gamma+\oint_{\partial\Omega}(\gamma-1)\frac{\bar{\rho}}{\bar{p}}\frac{\mathbf{m}}{\rho}\cdot\boldsymbol{\sigma}\cdot\mathbf{n}\,d\Gamma$$
$$+\oint_{\partial\Omega}(\gamma-1)\left(\frac{\bar{\rho}}{\bar{p}}-\frac{\rho}{p}\right)Pe^{-1}\nabla T\cdot\mathbf{n}\,d\Gamma. \tag{44}$$

For $\partial\Omega=\partial\Omega_{in}\cup\partial\Omega_{wall}\cup\partial\Omega_{out}$, where $\partial\Omega_{in}$, $\partial\Omega_{wall}$ and $\partial\Omega_{out}$ are the boundary segments along which $\mathbf{m}\cdot\mathbf{n}<0$, $\mathbf{m}\cdot\mathbf{n}=0$ and $\mathbf{m}\cdot\mathbf{n}>0$ respectively, expression (44) becomes in expanded form

$$\frac{dS}{dt} \leqslant -\int_{\partial\Omega_{in}} \frac{\mathbf{m}}{\rho}\cdot\mathbf{n}[V(q)-(\gamma-1)\bar{\rho}]\,d\Gamma+\int_{\partial\Omega_{in}}(\gamma-1)\frac{\bar{\rho}}{\bar{p}}\frac{\mathbf{m}}{\rho}\cdot\boldsymbol{\sigma}\cdot\mathbf{n}\,d\Gamma$$
$$+\int_{\partial\Omega_{in}}(\gamma-1)\left(\frac{\bar{\rho}}{\bar{p}}-\frac{\rho}{p}\right)Pe^{-1}\nabla T\cdot\mathbf{n}\,d\Gamma-\int_{\partial\Omega_{wall}}\frac{\mathbf{m}}{\rho}\cdot\mathbf{n}[V(q)-(\gamma-1)\bar{\rho}]\,d\Gamma$$
$$+\int_{\partial\Omega_{wall}}(\gamma-1)\frac{\bar{\rho}}{\bar{p}}\frac{\mathbf{m}}{\rho}\cdot\boldsymbol{\sigma}\cdot\mathbf{n}\,d\Gamma+\int_{\partial\Omega_{wall}}(\gamma-1)\left(\frac{\bar{\rho}}{\bar{p}}-\frac{\rho}{p}\right)Pe^{-1}\nabla T\cdot\mathbf{n}\,d\Gamma$$
$$-\int_{\partial\Omega_{out}}\frac{\mathbf{m}}{\rho}\cdot\mathbf{n}[V(q)-(\gamma-1)\bar{\rho}]\,d\Gamma+\int_{\partial\Omega_{out}}(\gamma-1)\frac{\bar{\rho}}{\bar{p}}\frac{\mathbf{m}}{\rho}\cdot\boldsymbol{\sigma}\cdot\mathbf{n}\,d\Gamma$$
$$+\int_{\partial\Omega_{out}}(\gamma-1)\left(\frac{\bar{\rho}}{\bar{p}}-\frac{\rho}{p}\right)Pe^{-1}\nabla T\cdot\mathbf{n}\,d\Gamma. \tag{45}$$

Expression (45) is instrumental in deriving suitable Navier–Stokes system boundary conditions that allow satisfying the hypotheses of Theorem 1 and thereby guarantee solution stability in the bounded energy sense. Note that this expression depends upon the momentum flux, deviatoric tractions and heat flux, in strict correspondence with terms in the weak statement (23)–(25). Consequently, the extracted boundary conditions constrain the values of these terms and are directly enforceable in (23)–(25). Note also that expressing p via state equation (5) leads to the equality

$$\int_{\Omega_{in}}\frac{\mathbf{m}}{\rho}\cdot\mathbf{n}[V(q)-(\gamma-1)\bar{\rho}]\,d\Gamma=$$
$$\int_{\Omega_{in}}\frac{\mathbf{m}}{\rho}\cdot\mathbf{n}\left\{\rho\left[\gamma\log\left(\frac{\rho}{\bar{\rho}}\right)-\log\left(\frac{(\gamma-1)(e-m_i m_i/2\rho)}{\bar{p}}\right)+(\gamma-1)\frac{\bar{\rho}}{\rho}\frac{e}{p}-\gamma\right]\right\}d\Gamma \tag{46}$$

used in the derivation of the inlet conditions.

The functions $g(t, q)$ of Theorem 1 can be identified as

$$g(t, q(\mathbf{x}, t))=\int_{\Omega_{out}}\frac{\mathbf{m}}{\rho}\cdot\mathbf{n}[V(q)-(\gamma-1)\bar{\rho}]\,d\Gamma, \tag{47}$$

while the function $f(t, q(\mathbf{x}, t))$ corresponds to the sum of the remaining integrals. The following Navier–Stokes boundary conditions prevent the positive growth of these integrals. They further revert to admissible Euler equation system boundary conditions as $Re\to\infty$.

Subsonic inflow

$$\rho=\rho_{\text{in}}, \qquad e=e_{\text{in}}, \qquad \sigma_{ij}n_j=a_{ij}\frac{\mathbf{m}}{\rho}\cdot\mathbf{s}_j+g_i, \tag{48}$$

where $\mathbf{s}_j$, $1\leqslant j\leqslant n-1$, is the unit tangent vector (pair) on $d\Gamma$ with unit normal $\mathbf{n}$. Note that (48) constitutes a Robin mixed boundary condition statement for the momentum equations for any finite Re. The rank of the matrix $[a_{i1}, a_{i2}, g_i]$ must be $n-1$ so that (48) reduces to $n+1$ boundary conditions as $Re\to\infty$. Further, the matrices a_{ij} must be bounded negative definite and the column matrix g_i must be a bounded function. This choice is valid since for subsonic flows

$$\frac{m_i m_i}{\rho}<\gamma p, \quad \text{hence } m_i m_i<\frac{\gamma(\gamma-1)}{\gamma+1}e\rho. \tag{49}$$

Consequently, both $\mathbf{m}\cdot\mathbf{n}$ and T are bounded since both ρ and e are constrained.

Supersonic inflow

$$\rho=\rho_{\text{in}}, \qquad e=e_{\text{in}}, \qquad \mathbf{m}=\mathbf{m}_{\text{in}}. \tag{50}$$

This choice is valid since it leads to bounded inflow integrals.

Wall boundaries

$$\mathbf{m}\cdot\mathbf{n}=0 \quad \text{(inviscid flow)},$$

$$m_j=0, \quad \forall j, \qquad aT+\frac{\partial T}{\partial n}=g_T \quad \text{(viscous flow)}, \tag{51}$$

where $a<0$ and g_T is a bounded function. Note that in either instance (51) leads to bounded surface integrals on $\partial\Omega_{\text{wall}}$.

Concerning the outflow boundary conditions, these must lead to a positive function (47) as required by Theorem 1. The function is cast as

$$g(t, q(\mathbf{x}, t))=\int_{\partial\Omega_{\text{out}}}\mathbf{m}\cdot\mathbf{n}\left[\gamma\log\left(\frac{\rho}{\bar{\rho}}\right)-\log\left(\frac{p}{\bar{p}}\right)+(\gamma-1)\frac{\bar{\rho}}{\rho}\frac{e}{\bar{p}}-\gamma\right]d\Gamma \tag{52}$$

and is positive if the expression in square brackets remains positive since $(\mathbf{m}\cdot\mathbf{n})_{\text{out}}>0$. This requirement is met if the following sufficient conditions are satisfied:

$$\log\left(\frac{\rho}{\bar{\rho}}\right)>1, \quad \forall\rho_{\text{out}}, \tag{53}$$

$$\log\left(\frac{\bar{p}}{p}\right)>0, \quad \forall p_{\text{out}}. \tag{54}$$

Hence

$$\bar{\rho}<\frac{(\rho_{\min})_{\text{out}}}{(\text{log-base e})}, \tag{55}$$

$$\bar{p}>(p_{\max})_{\text{out}}. \tag{56}$$

The constraint on $\bar{\rho}$ is evidently satisfied without any additional Mach-number-dependent specification on outflow density. Conversely, the constraint on $\bar{p}$ is met for subsonic outflows

when an outlet pressure boundary condition is imposed. This is detailed in the sequel, where suitable specifications are introduced that contribute to the positivity of (52) and boundedness and/or negativity of the remaining outflow integrals in (45).

Subsonic outflow

$$\sigma_{ij}n_j=0, \qquad Pe^{-1}\left(aT+\frac{\partial T}{\partial n}\right)=0, \qquad p=p_{\text{out}}, \tag{57}$$

where $a\leqslant 0$. These constraints reduce to a single boundary condition on p as $Re\to\infty$. Note that the constant $\bar{p}$ in (54) and (56) exists since p_{out}, hence $(p_{\max})_{\text{out}}$, is constrained.

Supersonic outflow

$$\sigma_{ij}n_j=0, \qquad Pe^{-1}\left(aT+\frac{\partial T}{\partial n}\right)=0, \tag{58}$$

where $a\leqslant 0$. Note that these constraints vanish identically as $Re\to\infty$. Further, in this case also the constant $\bar{p}$ exists since p_{out} decreases with increasing supersonic Mach number.

In summary, (48), (50), (51), (57) and (58) specify constraints on the surface momentum flux, deviatoric tractions and heat flux vector. Note that no steady state solution q can exist if the heat flux surface integral in (44) does not asymptotically vanish in time. Since $T=p/\rho$, constraints (57) can be recast as

$$p=p_{\text{out}}, \tag{59}$$

$$Pe^{-1}\left[a\left(\frac{p}{\rho}\right)+\frac{\partial}{\partial n}\left(\frac{p}{\rho}\right)\right]=0 \tag{60}$$

for any finite Re. Considering that the outlet static density is determined via the continuity equation, these constraints are ultimately outlet pressure specifications which are linearly independent. Since the heat conduction operator is second-order-elliptic, thus requiring one boundary condition, either the second or third expression in (57) should be used within a viscous layer extending to an outlet. This algorithm implements the first expression in (57) coupled with either the second in (57) in such a region, or the third in (57) in essentially inviscid flow outlet regions. The numerical results to be discussed document the performance of this combination and support its validity.

The boundary conditions (48), (50), (51), (57) and (58) collectively prevent the positive growth of all integrals in (45) except the term

$$\int_{\partial\Omega_{\text{out}}}\frac{1}{\rho}(\mathbf{m}\cdot\mathbf{n})[V(q)-(\gamma-1)\bar{p}]\,d\Gamma>0, \tag{61}$$

which is allowed to vary. Consequently, the hypotheses of Theorem 1 are satisfied and therefore the solution q of (1), complemented by the derived boundary conditions, is bounded.

4.2. Implementation of boundary conditions

The enforcement of Dirichlet boundary conditions on the state variable q is a routine matter and is fully described in Reference 19. Concerning the other derived constraints, these are keyed to the weak statement surface integrals in (23)–(25). Specifically, to impose the wall tangency boundary condition (51), it is sufficient to delete the appropriate momentum flux surface integrals

in (23)–(25) that would otherwise be computed along any wall segment. Analogously, the deviatoric traction and heat flux boundary conditions are effectively enforced for all values of Re by replacing the arguments of the relevant integrals in (24) and (25) with expressions (48), (51), (57) and (58). In particular, the explicit presence of the static pressure p in (24) and (25) suggests a direct enforcement without augmenting these equations with an additional constraint, usually the time derivative of the state equation (5) set to zero.[6] The advantages of this procedure are twofold. First, the critical exit pressure boundary condition is 'extensively' enforced in the sense that it actively functions in the momentum and energy equations. Secondly, this procedure does not structurally modify the equation system to any degree. Very likely, these advantages translate into the overall monotonicity displayed by the TWS algorithm solutions to be discussed.

5. INITIAL CONDITIONS

To expeditiously attain a steady state, the solution initial field $q(\mathbf{x}, t_0)$ should model in some sense the final solution. For n-dimensional confined flow problems, computations can be initialized with the isentropic quasi-one-dimensional steady solution for ρ and e. For example, for $n=2$ the initial distribution for $(m_x)_{2D}$ is determined after establishing the initial values for $(m_y)_{2D}$. Expressing the quasi-1D continuity equation source term with the initial $(m_x)_{2D}$ and equating it with the partial derivative of $(m_y)_{2D}$ with respect to y yields

$$(m_x)_{2D}=(m_x)_{Q1D}\cos[\theta(y)], \tag{62}$$

$$\frac{(m_x)_{2D}}{A(x)}\frac{dA(x)}{dx}=\frac{\partial m_y}{\partial y}, \tag{63}$$

where $\theta(y)$ is the geometric angularity. Since $(m_x)_{Q1D}$ is a function of x only, and the variation of $\theta(y)$ is assumed to satisfy $\cos\theta\approx 1$, then the approximate direct integration of (63) yields

$$(m_y)_{2D}\approx\frac{(m_x)_{2D}}{A(x)}\frac{dA(x)}{dx}(y-y_T), \tag{64}$$

where y_T is the centre-plane ordinate along which $m_y=0$; see Figure 1.

Importantly, the distribution of $(m_y)_{2D}$ computed via (64) satisfies the wall tangency constraint, as is easily shown. Assume the geometric form is mathematically expressed as

$$A(x)=l(y_T-y_B), \tag{65}$$

where $l=1$ is the channel unit transverse width. Consequently,

$$\frac{1}{A(x)}\frac{dA(x)}{dx}(y-y_T)=-\frac{dy_B}{dx}\frac{(y-y_T)}{(y_T-y_B)}\equiv\tan[\theta(y)]; \tag{66}$$

therefore

$$(m_y)_{2D}=\left(-\frac{dy_B}{dx}\frac{(y-y_T)}{(y_T-y_B)}\right)(m_x)_{2D}=\tan[\theta(y)](m_x)_{2D}, \tag{67}$$

which, upon setting $y=y_B$, specializes to

$$m_y=m_x\tan[\theta(y)], \tag{68}$$

i.e. the wall tangency constraint. Finally, the corresponding $(m_x)_{2D}$ is obtained with (62) so that

$$(m_x)_{2D}^2+(m_y)_{2D}^2=(m_x)_{Q1D}^2. \tag{69}$$

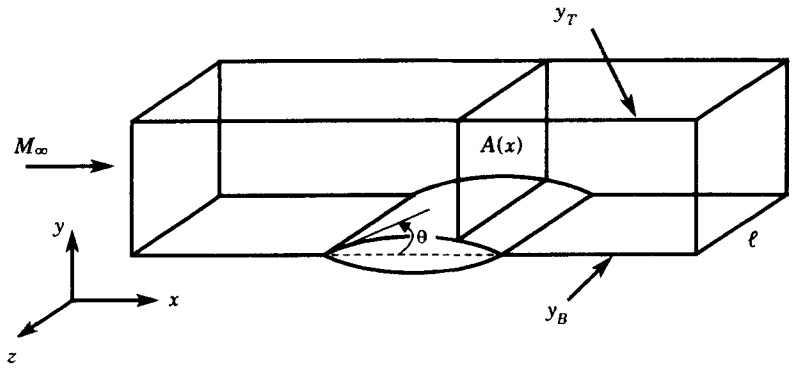

Figure 1. Internal flow domain geometry

For an external flow field problem the procedure is analogous. Specifically, one replaces y_T with an appropriate reference level y_R in (57) so that the values of $(m_y)_{2D}$, as obtained with $y = y_T$, correspond to an admissible outer boundary distribution for this momentum component.

6. FINITE ELEMENT SEMI-DISCRETIZATION

The finite element spatial semi-discrete approximations q^h, $\mathbf{f}^h$ and $\mathbf{f}^{vh}$ to the Navier–Stokes variables q, $\mathbf{f}$ and $\mathbf{f}^v$ respectively are constructed by projection of the solution q onto a finite-dimensional Sobolev subspace S_M of the Hilbert space S^m of all admissible trial functions. In this study the Galerkin criterion is used, hence the test functions w (see (22)) are the identical members of S_M. Further, the semi-discretization Ω^h of the solution domain Ω, i.e.

$$\Omega^h \equiv \bigcup_e^{M_e} \Omega_e, \tag{70}$$

is obtained by subdividing Ω into M_e quadrilateral finite elements each denoted Ω_e.

Inserting q^h as well as $\mathbf{f}^h$ and $\mathbf{f}^{vh}$ in (23)–(25) yields the finite element semi-discrete statement

$$\sum_{e=1}^{M_e} \left(\int_{\Omega_e} w \frac{\partial q^h}{\partial t} \mathrm{d}\Omega - \int_{\Omega_e} \nabla w \cdot \mathbf{f}^h \, \mathrm{d}\Omega + \int_{\Omega_e} \nabla w \cdot \mathbf{f}^{vh} \, \mathrm{d}\Omega \right.$$
$$\left. + \oint_{\partial\Omega_e} w \mathbf{f}^h \cdot \mathbf{n} \, \mathrm{d}\Gamma - \oint_{\partial\Omega_e} w \mathbf{f}^{vh} \cdot \mathbf{n} \, \mathrm{d}\Gamma + \mathrm{B} \int_{\hat{\Omega}_e} \nabla_\eta w \cdot \nabla_\eta q^h \, \mathrm{d}\eta \right) = 0, \tag{71}$$

where $\hat{\Omega}_e$ is the image of each element Ω_e in the computational space η and $\nabla_\eta \equiv \partial/\partial\eta_l$. The chosen subspace S_M is formed by unions of bilinear Lagrange polynomials of the local element co-ordinates η. These unions are the generalized hat functions $N_i(\eta)$ which attain the value unity at node $\mathbf{x}^i$ and zero at all other nodes, have support on all the elements that share $\mathbf{x}^i$ and identically vanish on all other elements elsewhere in Ω^h. Consequently, for time and space separability, the semi-discrete expansion for q^h is

$$q^h(\mathbf{x}(\eta), t) = \sum_{l=1}^{M} N_l(\eta) q^l(t), \tag{72}$$

where M is the total number of nodes in Ω^h and $q^l(t)$ denotes the time-dependent expansion coefficient at node l. Analogously, the expansions for $\mathbf{f}^h$ and $\mathbf{f}^{vh}$ in terms of Cartesian components are

$$\mathbf{f}^h \Rightarrow f_j^h \equiv \begin{Bmatrix} N_l m_j^l(t) \\ u_j^k(t) N_k N_l m_i^l(t) + N_l p^l(t) \delta_{ij} \\ u_j^k(t) N_k N_l (e^l(t) + p^l(t)) \end{Bmatrix}, \tag{73}$$

$$\mathbf{f}^{vh} \Rightarrow f_j^{vh} \equiv \begin{Bmatrix} 0 \\ \dfrac{1}{Re}\left(\dfrac{\partial N_l}{\partial x_j} u_i^l(t) + \dfrac{\partial N_l}{\partial x_i} u_j^l(t) - \dfrac{2}{3}\dfrac{\partial N_l}{\partial x_r} u_r^l(t)\delta_{ij}\right) \\ \dfrac{u_i^k(t) N_k}{Re}\left(\dfrac{\partial N_l}{\partial x_j} u_i^l(t) + \dfrac{\partial N_l}{\partial x_i} u_j^l(t) - \dfrac{2}{3}\dfrac{\partial N_l}{\partial x_r} u_r^l(t)\delta_{ij}\right) + \dfrac{1}{Pe}\dfrac{\partial N_l}{\partial x_j} T^l(t) \end{Bmatrix}, \tag{74}$$

where

$$u_j^l(t) \equiv m_j^l(t)/\rho^l(t). \tag{75}$$

Note that a double interpolation is used to discretize the convection terms rather than employing the 'group approximation'.[9] This reduces the formal interpolation error and is verified to yield an appropriate improvement in solution accuracy, especially around shocks.

The co-ordinate transformation from Cartesian to curvilinear co-ordinates is accommodated in each integral in (71), and for the isoparametric procedure[19] is expressed via a relation analogous to (72) as

$$\mathbf{x} = \sum_{i=1}^{M} N_l(\boldsymbol{\eta}) \mathbf{x}^l, \tag{76}$$

where $\boldsymbol{\eta} \in [-1; +1] \times [-1; +1]$ spans each Ω_e where N_l is supported. Thereafter, the relation between the partial derivatives with respect to η_i and x_j and its inverse are

$$\left\{\frac{\partial}{\partial \eta_i}\right\} = \left[\frac{\partial x_j}{\partial \eta_i}\right]\left\{\frac{\partial}{\partial x_j}\right\} \tag{77}$$

and

$$\left\{\frac{\partial}{\partial x_i}\right\} = [J]^{-1}\left\{\frac{\partial}{\partial \eta_j}\right\} = \frac{1}{\det J}[e_{ij}]\left\{\frac{\partial}{\partial \eta_j}\right\}, \tag{78}$$

where $[J]$ denotes the Jacobian matrix with entries $\partial x_j/\partial \eta_i$ and determinant $\det J$, and e_{ij} are the elements in the matrix $(\det J)[J]^{-1}$. Further, the area differential $d\Omega$ is recast as

$$d\Omega = (\det J)\, d\boldsymbol{\eta}. \tag{79}$$

Expressions (72)–(75) as well as (78) and (79) are then inserted in (71) to allow the explicit evaluation on each Ω_e. Finally, the terminal ordinary differential equation system is expressed at

the representative node r as

$$\int_{\hat{\Omega}} N_r N_l \frac{\mathrm{d}\rho^l}{\mathrm{d}t}(\det J)\,\mathrm{d}\eta - \int_{\hat{\Omega}} e_{jk}\frac{\partial N_r}{\partial \eta_k} N_l m_j^l(t)\,\mathrm{d}\eta + \beta_\rho \int_{\hat{\Omega}} |\mathbf{u}^s(t)|\, N_s \frac{\partial N_r}{\partial \eta_l}\frac{\partial N_k}{\partial \eta_l}\rho^k(t)\,\mathrm{d}\eta = 0, \tag{80}$$

$$\begin{aligned}\int_{\hat{\Omega}} N_r N_l \frac{\mathrm{d}m_i^l}{\mathrm{d}t}(\det J)\,\mathrm{d}\eta &- \int_{\hat{\Omega}} u_j^s(t) N_s e_{jk}\frac{\partial N_r}{\partial \eta_k} N_l m_i^l(t)\,\mathrm{d}\eta - \int_{\hat{\Omega}} e_{jk}\frac{\partial N_r}{\partial \eta_k} N_l p^l(t)\delta_{ij}\,\mathrm{d}\eta \\ &+ \frac{1}{Re}\int_{\hat{\Omega}} \frac{e_{jk}}{\det J}\frac{\partial N_r}{\partial \eta_k}\left(e_{js}\frac{\partial N_l}{\partial \eta_s}u_i^l(t) + e_{is}\frac{\partial N_l}{\partial \eta_s}u_j^l(t) - \frac{2}{3}e_{ks}\frac{\partial N_l}{\partial \eta_s}u_k^l(t)\delta_{ij}\right)\mathrm{d}\eta \\ &+ \beta_{m_i}\int_{\hat{\Omega}} |\mathbf{u}^s(t)|\, N_s \frac{\partial N_r}{\partial \eta_l}\frac{\partial N_k}{\partial \eta_l} m_i^k(t)\,\mathrm{d}\eta = 0,\end{aligned} \tag{81}$$

$$\begin{aligned}\int_{\hat{\Omega}} N_r N_l \frac{\mathrm{d}e^l}{\mathrm{d}t}(\det J)\,\mathrm{d}\eta &- \int_{\hat{\Omega}} u_j^s(t) N_s e_{jk}\frac{\partial N_r}{\partial \eta_k} N_l (e^l(t) + p^l(t))\,\mathrm{d}\eta \\ &+ \frac{1}{Re}\int_{\hat{\Omega}} u_i^g(t) N_g \frac{e_{jk}}{\det J}\frac{\partial N_r}{\partial \eta_k}\left(e_{js}\frac{\partial N_l}{\partial \eta_s}u_i^l(t) + e_{is}\frac{\partial N_l}{\partial \eta_s}u_j^l(t) - \frac{2}{3}e_{ks}\frac{\partial N_l}{\partial \eta_s}u_k^l(t)\delta_{ij}\right)\mathrm{d}\eta \\ &+ \frac{1}{Pe}\int_{\hat{\Omega}} \frac{e_{jk}}{\det J}\frac{\partial N_r}{\partial \eta_k}e_{js}\frac{\partial N_l}{\partial \eta_s}T^l(t)\,\mathrm{d}\eta + \beta_e\int_{\hat{\Omega}} |\mathbf{u}^s(t)|\, N_s \frac{\partial N_r}{\partial \eta_l}\frac{\partial N_k}{\partial \eta_l} e^k(t)\,\mathrm{d}\eta = 0,\end{aligned} \tag{82}$$

where $\hat{\Omega}$ is the image of Ω^h in the computational space η.

The boundary values of the semi-discrete pressure p^l in (81) and (82) are enforced as follows. With reference to Figure 2, the prescribed values of pressure along nodal line '$l+1$' replace the values $p^m(t)$ in the formation of (81) and (82). This replacement affects all semi-discrete equations assembled at each node on line '$l+1$', and also every equation formulated at each node at line 'l' since these also couple nodes 'm'. Moreover, the known pressure values are also inserted in the appropriate Jacobian contributions, in the implicit integration, and therein $(\partial p^h/\partial q^h)_{\text{out}}$ is set to zero. The numerical results support the validity of this operational procedure.

Given that accurate solutions of the Navier–Stokes equations demand refined grids, a convenient and cost-effective approximate evaluation of each integral in (80)–(82) is obtained by

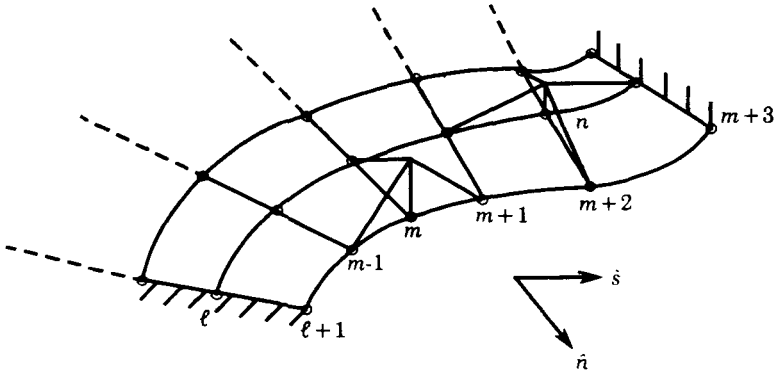

Figure 2. Illustration of outflow pressure imposition

assuming piecewise constant metric data which, consequently, are extracted from each integral. This procedure is exemplified by the following representative term:

$$\int_{\hat{\Omega}_e} e_{jk}(\eta)\frac{\partial N_r}{\partial \eta_k}N_l m_j^l(t)\,\mathrm{d}\eta \approx e_{jk}(\mathbf{o})\int_{\hat{\Omega}_e}\frac{\partial N_r}{\partial \eta_k}N_l\,\mathrm{d}\eta\; m_j^l(t) = e_{jk}(\mathbf{o})\,\{\text{array}\}\,\{m_j^l(t)\}. \tag{83}$$

Here $e_{jk}(\mathbf{o})$ is the metric data element evaluated at the element centroid and {array} denotes the (Cartesian element shape-independent) data resulting from the remaining integral.[19] This evaluation procedure, which is illustrated by (83) and also involves usage of centroidal evaluations of $\det J$, is extended to all metric data in (80)–(82). This technique permits extraction of all metric data from the associated integrals. Consequently, the terminal system formation requires only a few spatial integrations which are exactly carried out once and for all as a preprocessor operation. Thereby, the compute-intensive element-by-element numerical integration at each time level is totally eliminated, hence the resulting procedure becomes competitive with difference-coding methodology.

7. ORDINARY DIFFERENTIAL EQUATION SYSTEM AND IMPLICIT RUNGE–KUTTA INTEGRATION

Equations (80)–(82) constitute the finite element semi-discretization which yields the *global order* ordinary differential equation (ODE). The ODE statement for a 2D domain Ω^h is

$$\mathscr{M}\frac{\mathrm{d}\tilde{q}}{\mathrm{d}t}+\tilde{f}_1(\tilde{q})+\tilde{f}_2(\tilde{q})=0, \tag{84}$$

where $\mathscr{M}$ is the semi-discretization mass matrix and $\tilde{q}$ is the array of nodal values of q^h. Note that each entry in this array consists of four components. Concurrently, the array $\tilde{f}_l$ defines the sum of the discretized η_l partial derivatives of the inviscid, viscous and dissipation fluxes.

The usual implicit time algorithms for the integration of (84) are the one-stage 'theta algorithms',[1,2,6] which, in a one-iteration mode, yield the *delta-form* terminal matrix statement

$$\left[\mathscr{M}+\theta\Delta t\left[\frac{\partial\tilde{f}_1}{\partial\tilde{q}}\right]_n+\theta\Delta t\left[\frac{\partial\tilde{f}_2}{\partial\tilde{q}}\right]_n\right]k_1=-\Delta t(\tilde{f}_1(\tilde{q}_n)+\tilde{f}_2(\tilde{q}_n)),$$

$$\tilde{q}_{n+1}=\tilde{q}_n+k_1, \tag{85}$$

where n indicates the discrete time station. For $\theta\geqslant 0{\cdot}5$ this algorithm family is unconditionally stable with respect to the linear model problem

$$\mathrm{d}q/\mathrm{d}t=\lambda_1 q. \tag{86}$$

Specifically, $\theta=1$ yields the backwards Euler rule, which allows quick convergence to steady state even though it is only first-order-accurate. Conversely, $\theta=\frac{1}{2}$ leads to a second-order-accurate algorithm, the Crank–Nicolson rule, which, however, does not afford the same convergence rate as backwards Euler. Therefore, in order to have the desirable features of each of the mentioned algorithms in a single procedure, an implicit Rosenbrock–Runge–Kutta (IRK)[26–34] scheme has been developed.[17] This algorithm expands the range of stable integration steps permitted by the backwards Euler rule and maintains second-order accuracy in time by integrating (84) with the

solution sequence:

$$\left[\mathscr{M}+\alpha\Delta t\left[\frac{\partial\tilde{f}_1}{\partial\tilde{q}}\right]_n+\alpha\Delta t\left[\frac{\partial\tilde{f}_2}{\partial\tilde{q}}\right]_n\right]k_1=-\Delta t(\tilde{f}_1(\tilde{q}_n)+\tilde{f}_2(\tilde{q}_n)),$$

$$\left[\mathscr{M}+\alpha\Delta t\left[\frac{\partial\tilde{f}_1}{\partial\tilde{q}}\right]_n+\alpha\Delta t\left[\frac{\partial\tilde{f}_2}{\partial\tilde{q}}\right]_n\right]k_2=-\Delta t(\tilde{f}_1(\tilde{q}_n+\beta_{21}k_1)+\tilde{f}_2(\tilde{q}_n+\beta_{21}k_1)),$$

$$\tilde{q}_{n+1}=\tilde{q}_n+c_1k_1+c_2k_2. \tag{87}$$

This time algorithm has been analysed[17] and the results indicate that it is indeed optimally second-order-accurate and non-linearly stiffly stable. This effective combination is attained by selecting the IRK procedure coefficients so that the scheme is second-order-accurate and the magnitude of its amplification ratio for the non-linear model equation

$$dq/dt=\lambda_1q+\lambda_2q^2 \tag{88}$$

is less than unity and decays as the system characteristic eigenvalues grow unboundedly. Therefore, reliable unsteady simulations can be afforded without imposing severe restrictions on the time step. Concurrently, expeditious attainment of a steady state (when one exists) can also be obtained, as the documentary results will confirm.

Note the important feature that no iteration is defined; instead, (87) constitutes a two-stage non-iterative procedure for establishing the arrays k_1 and k_2, hence $\tilde{q}_{n+1}$. The optimal values of the IRK scalar parameters are

$$\begin{aligned}\alpha&=0{\cdot}292\,893\,219, & \beta_{21}&=0{\cdot}435\,281\,374,\\ c_1&=0{\cdot}573\,223\,304, & c_2&=0{\cdot}426\,776\,696.\end{aligned} \tag{89}$$

Note also that with the following determination,

$$\begin{aligned}\alpha&=\theta, & \beta_{21}&=0,\\ c_1&=1, & c_2&=0,\end{aligned} \tag{90}$$

(87) yields the implicit θ-algorithms (86).

8. TENSOR MATRIX PRODUCT APPROXIMATION FACTORIZATION

The solution of (87) at time level $n+1$ is obtained in practice using a tensor matrix product approximate factorization of the IRK Jacobian matrices. This replaces the defined large sparse matrices with an efficient sequence of banded matrix operations.[1,21–23] Hence each linear system in (87) is recast as

$$\left[\mathscr{M}_1+\alpha\Delta t\left[\frac{\partial\tilde{f}_1}{\partial\tilde{q}}\right]_n\right]\otimes\left[\mathscr{M}_2+\alpha\Delta t\left[\frac{\partial\tilde{f}_2}{\partial\tilde{q}}\right]_n\right]k_i=-\Delta t\sum_{l=1}^{2}\tilde{f}_l(\tilde{q}_n+\beta_{21}k_1\delta_i^2),\quad 1\leqslant i\leqslant 2, \tag{91}$$

where $\otimes$ denotes the matrix tensor product.[19] Each matrix component contains decoupled inner blocks that correspond to the Jacobians of the semi-discrete equations formulated at the nodes on independent grid lines. Hence, as indicated by the subscripts 1 and 2 in (91), the two component matrices are formed using strictly one-dimensional operators associated to the curvilinear co-ordinates η_1 and η_2. Significantly, each matrix always remains block-tridiagonal whatever the order and bandwidth of the associated multidimensional matrix are.[1,21–23] The approximate

solution for system (91) is obtained with the sequence

$$\left[\mathscr{M}_1+\alpha\Delta t\left[\frac{\partial\tilde{f}_1}{\partial\tilde{q}}\right]_n\right]l_i=-\Delta t\sum_{l=1}^{2}\tilde{f}_l(\tilde{q}_n+\beta_{21}k_1\delta_i^2),$$

$$\left[\mathscr{M}_2+\alpha\Delta t\left[\frac{\partial\tilde{f}_2}{\partial\tilde{q}}\right]_n\right]k_i=l_i,\quad 1\leqslant i\leqslant 2. \tag{92}$$

Noting in (92) the subscript range for i, the IRK solution arrays are specifically computed by the following steps.

1. Form $[\mathscr{M}_1+\alpha\Delta t[\partial\tilde{f}_1/\partial\tilde{q}]_n]$ and $-\Delta t\Sigma_{l=1}^{2}\tilde{f}_l(\tilde{q}_n+\beta_{21}k_1\delta_i^2)$ along co-ordinate curves in the η_1-direction, enforce appropriate boundary conditions and solve for the intermediate array l_1.
2. Form $[\mathscr{M}_2+\alpha\Delta t[\partial\tilde{f}_2/\partial\tilde{q}]_n]$ along co-ordinate curves in the η_2-direction, enforce appropriate boundary conditions and solve for the intermediate array k_1.
3. Repeat steps 1 and 2 for $i=2$, hence determine k_2.

Additional details are given in Reference 34.

9. DISCUSSION AND RESULTS

Numerical verifications have focused on benchmark quasi-1D shocked inviscid flows and 2D transonic inviscid and viscous flows. The computational results confirm the effectiveness of the TWS algorithm dissipation mechanism to counter the spatial semi-discretization dispersive error as well as the developed boundary conditions and relevant implementation. They also document the relative accuracy and stability of the backwards Euler (EU), trapezoidal/Crank–Nicolson rule (CN) and implicit Runge–Kutta (IRK) algorithms.

9.1. Quasi-one-dimensional solutions

The de Laval nozzle geometry and test problem specification of Liou and van Leer[6] have been utilized for this test. The computational experiment boundary conditions are $\rho(0,t)=\rho_{\text{in}}$, $e(0,t)=e_{\text{in}}$ and $p(L,t)=p_{\text{out}}$. Solutions were generated using various constant integration time steps $0{\cdot}005\leqslant\Delta t\leqslant 0{\cdot}3$, corresponding to the range $0{\cdot}65\leqslant\text{CFL}_{\max}\leqslant 35$. The initial condition was steady state isentropic subsonic flow throughout.

An appropriate specification to evaluate accuracy and stability is for an impulsive change from the steady subsonic state, as accomplished by a step decrease in exit pressure p_{out} at $t=0$. The resultant rarefaction propagates upstream as an expansion wave which, upon reaching the nozzle throat, triggers the development of a normal shock wave. Liou and van Leer's steady state problem definition parameters are

$$M_{\text{in}}=0{\cdot}24,\qquad p_{\text{out}}/p_{\text{total in}}=0{\cdot}84, \tag{93}$$

and the theoretical steady state predicts a normal shock at location $x/L=0{\cdot}65$ with shock Mach number $M_s=1{\cdot}40$. Figure 3 sketches the nozzle geometry with cross-sectional area distribution

$$A(x)=\begin{cases}1{\cdot}75-0{\cdot}75\cos[(x-0{\cdot}5)\pi/0{\cdot}5], & 0{\cdot}0\leqslant x\leqslant 0{\cdot}5,\\ 1{\cdot}25-0{\cdot}25\cos[(x-0{\cdot}5)\pi/0{\cdot}5], & 0{\cdot}5\leqslant x\leqslant 1{\cdot}0.\end{cases} \tag{94}$$

A uniform $M=100$ node spatial discretization was employed, in concert with a linear trial space finite element implementation of the Taylor weak statement (TWS) semi-discrete formulation.

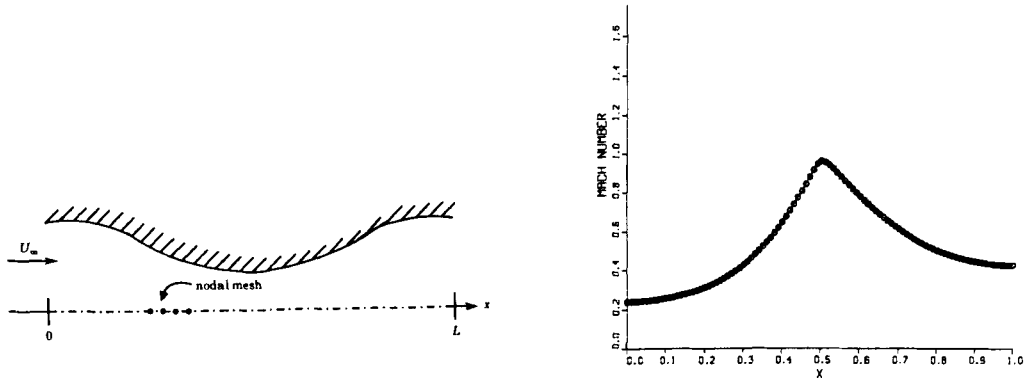

Figure 3. De Laval nozzle and initial condition Mach number profile

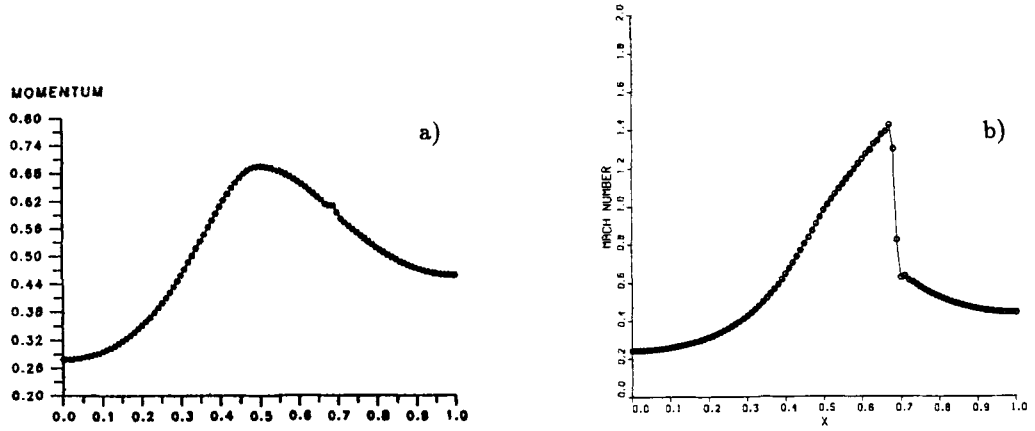

Figure 4. TWS finite element quasi-1D Euler algorithm steady state solution, $M_s \simeq 1{\cdot}40$: (a) momentum; (b) Mach number

The TWS steady state solution is graphically summarized in Figures 4(a) and 4(b) as momentum and Mach number distributions respectively. Convergence to steady state using the IRK algorithm was achieved within 60 steps for the dynamically optimized TWS dissipation parameter set $\beta_q = 0{\cdot}164[1{\cdot}00, 0{\cdot}93, 0{\cdot}98]$. The fully discrete nodal solution is essentially non-oscillatory (ENO) and the shock is quite crisp, being captured within three elements. Furthermore, its location and upstream Mach number are accurately predicted (Figure 4(b)) and the associated discrete approximation to the Rankine–Hugoniot jump condition is clearly evident in Figure 4(a).

For comparison, Figure 5 displays the solution Mach distributions published by Liou and van Leer as obtained using several first- and second-order-accurate flux-splitting algorithms. They report that steady state convergence is achieved within 159 time steps using the backwards Euler rule. The first-order van Leer splitting appears to be the only procedure that yields a solution devoid of the shock precursory overshoots present in all second-order solutions. Comparing Figures 4 and 5 thus verifies that the selected TWS semi-discrete algorithm can yield accurate results for the problem class to be addressed. Hence a time-accurate evolution will be affected principally by Δt and the chosen time algorithm.

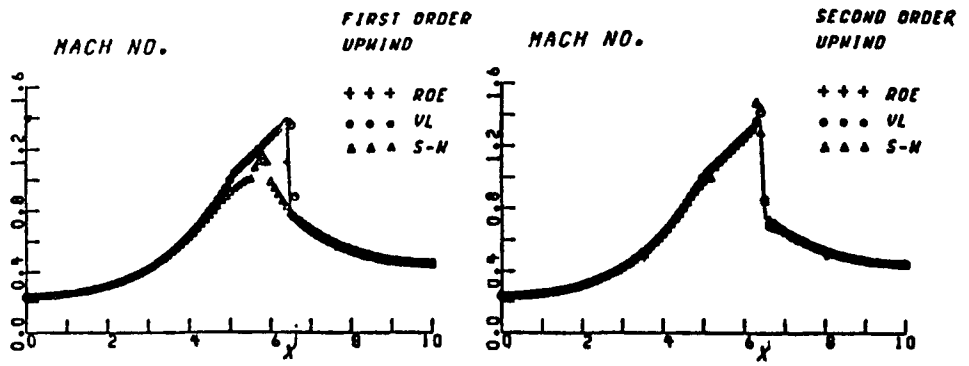

Figure 5. Quasi-1D Euler steady state solutions, various flux splitting algorithm solutions, from Liou and van Leer[6]

Next, the unsteady solution evolutions obtained by each time algorithm are quantitatively compared at a specified time station and for various time step sizes for the de Laval nozzle problem. Figures 6(a)–6(f) summarize the reference time-accurate solution in terms of the Mach number distribution as obtained at six pertinent time stations. This is computed using the IRK algorithm with $\Delta t = 0{\cdot}005$ s, which renders the time truncation error negligible. Specifically, Figures 6(a)–6(c) illustrate the upstream propagation of the expansion wave travelling towards the throat as caused by the step decrease in exit pressure. The flow then chokes and a normal shock wave forms and strengthens in moving downstream as indicated in Figure 6(e). The nodal solution is ENO throughout, with a crisp shock which is captured across three elements at station $t = 1{\cdot}8$ s and only two elements at station $t = 2{\cdot}8$ s. At these two time levels the shock Mach numbers are $M_s = 1{\cdot}220$ and $M_s = 1{\cdot}330$ respectively. Figures 7(a)–7(c) graph the associated density, momentum and pressure solutions respectively at $t = 1{\cdot}8$ s.

This solution sequence was then repeated to compare Mach number distributions at time levels $t = 1{\cdot}0$ and $1{\cdot}8$ s as computed with $0{\cdot}2 \leqslant \Delta t \leqslant 0{\cdot}3$ s. Figures 8(a)–8(c) are associated with Figure 6(b) and compare the three algorithm solutions obtained at $t = 1{\cdot}0$ s using $\Delta t = 0{\cdot}2$ s. The shock has not yet formed and the accurate peak Mach number is $M_p = 0{\cdot}95$. The presence of the rarefaction wave is better defined in the IRK solution and the computed Mach number is indeed $M_p = 0{\cdot}95$. The trapezoidal rule also yields $M_p = 0{\cdot}95$ but displays an unacceptable outlet oscillation. Conversely, the backwards Euler solution reaches $M_p = 0{\cdot}99$ and is overly diffused, hence inaccurate.

Figures 9(a)–9(c) are associated with Figure 6(e) and compare the nodal Mach number solutions at time level $t = 1{\cdot}8$ s as obtained using $\Delta t = 0{\cdot}2$ s for each of the three integration algorithms. The accurate shock Mach numbers are $M_{s1} = 1{\cdot}220$ and $M_{s2} = 0{\cdot}824$. The backwards Euler solution is monotone; however, the shock is overly diffused, since the Mach number distribution smoothly curves to negotiate the discontinuity, and the shock Mach numbers are $M_{s1} = 1{\cdot}86$ and $M_{s2} = 0{\cdot}848$. In contrast, the trapezoidal rule shows a sharper shock characterized by accurate shock Mach numbers. However, the post-shock solution is distorted and oscillatory, hence unacceptable. In distinction, the IRK solution remains ENO, with a crisp shock with correct shock Mach numbers.

Finally, Figures 10(a)–10(c) show the Mach number solution at time level $t = 1{\cdot}8$ s but now determined employing $\Delta t = 0{\cdot}3$ s for each procedure. All three solutions undergo a decrease in time accuracy. The backwards Euler solution is thoroughly diffused; the shock now is spread over four elements and the relevant shock Mach numbers are $M_{s1} = 1{\cdot}10$ and $M_{s2} = 0{\cdot}818$. The

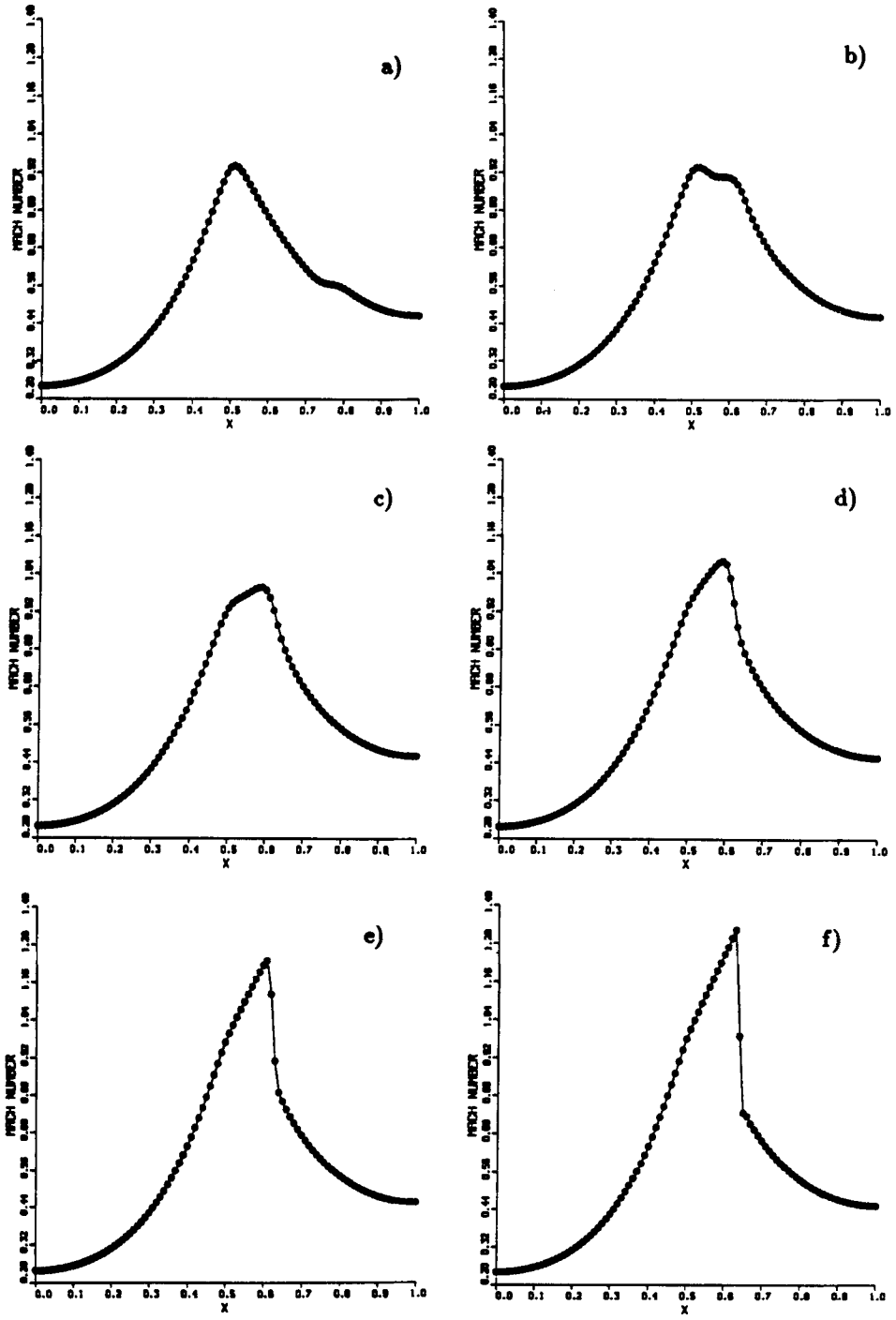

Figure 6. Unsteady quasi-1D Euler solution, implicit Runge–Kutta, Mach number profiles, $\Delta t = 0{\cdot}005$ s: (a) $t = 0{\cdot}4$ s; (b) $t = 1{\cdot}0$ s; (c) $t = 1{\cdot}2$ s; (d) $t = 1{\cdot}4$ s; (e) $t = 1{\cdot}8$ s; (f) $t = 2{\cdot}8$ s

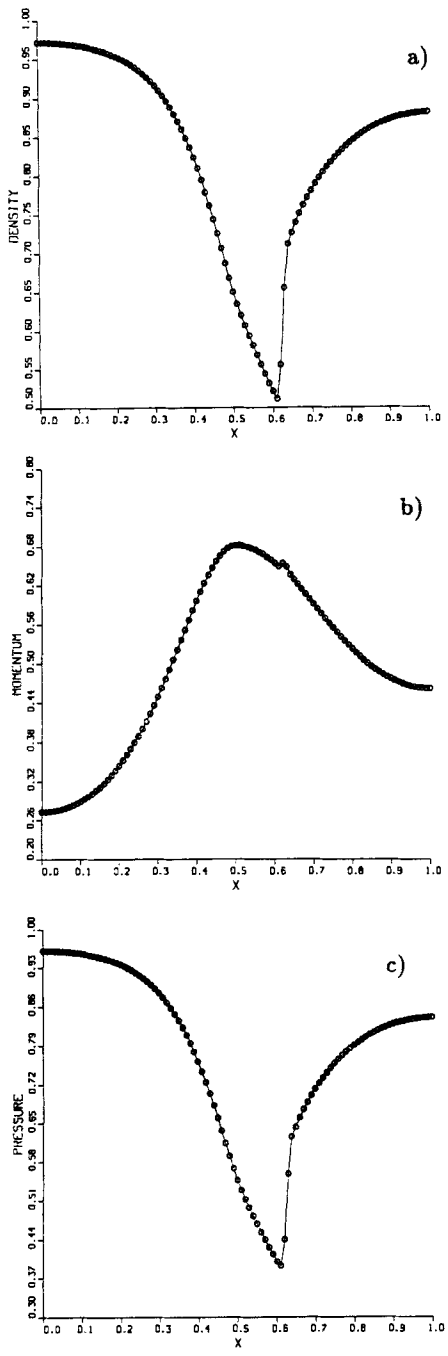

Figure 7. Unsteady quasi-1D Euler solution, implicit Runge–Kutta, $\Delta t = 0{\cdot}005$ s, $t = 1{\cdot}8$ s: (a) density; (b) momentum; (c) pressure

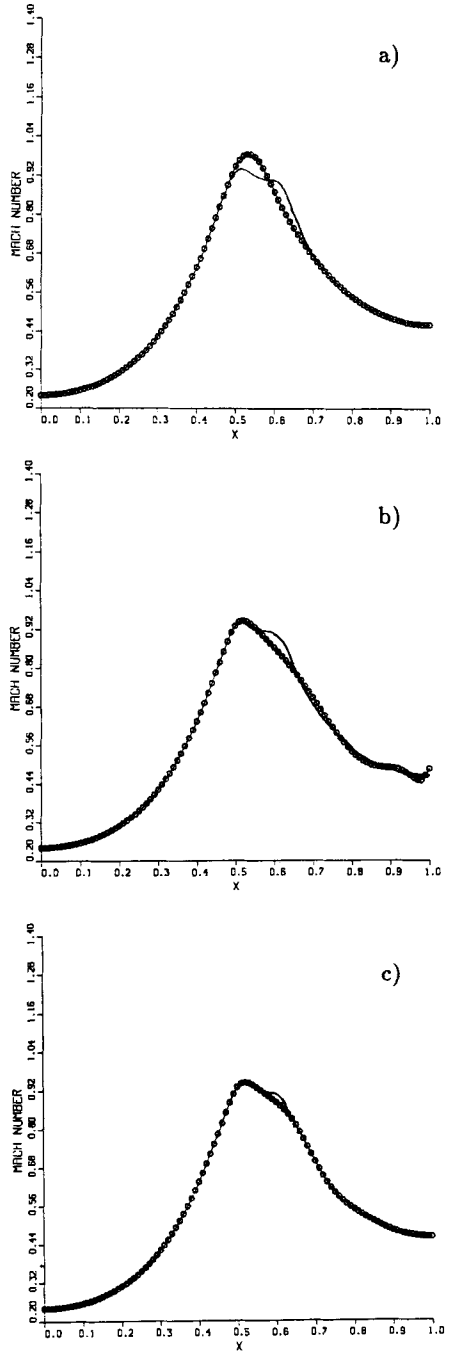

Figure 8. Unsteady quasi-1D Euler solution, $t = 1{\cdot}0$ s, $\Delta t = 0{\cdot}2$ s: ——, from Figure 6(b); (a) EU; (b) CN; (c) IRK

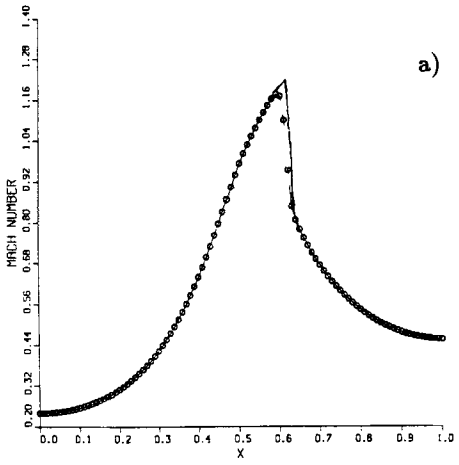

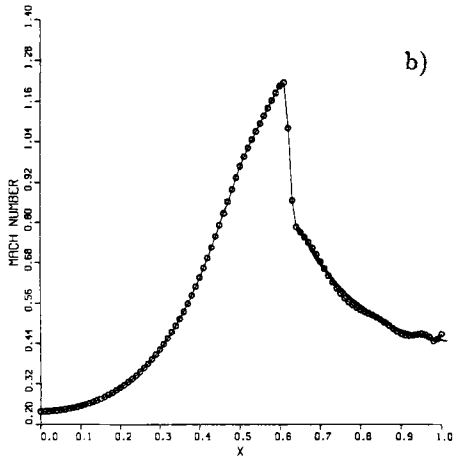

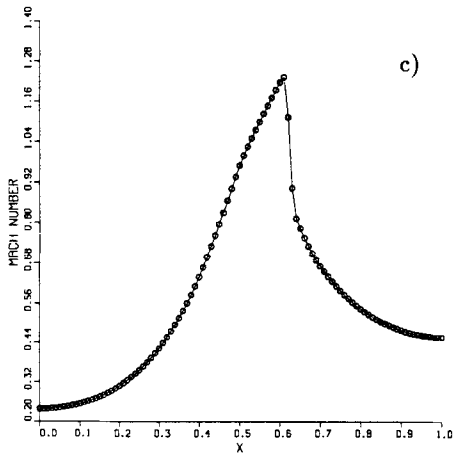

Figure 9. Unsteady quasi-1D Euler solution, $t = 1{\cdot}8$ s, $\Delta t = 0{\cdot}2$ s: ——, from Figure 6(e); (a) EU; (b) CN; (c) IRK

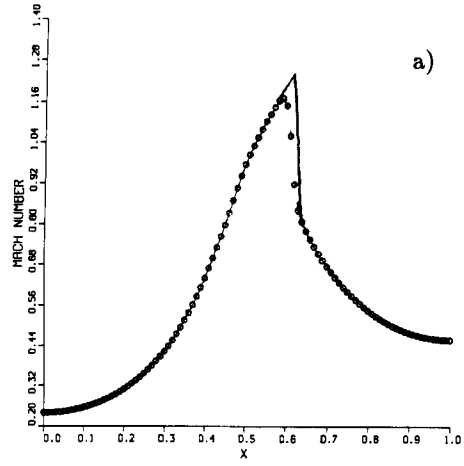

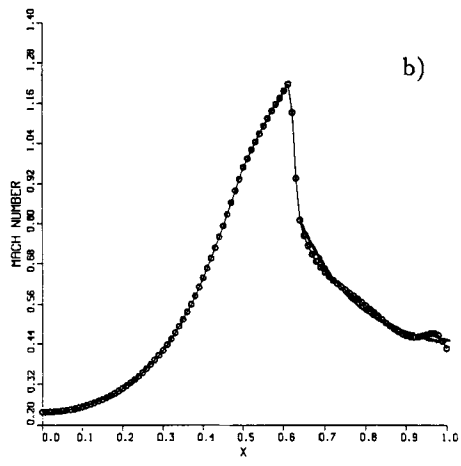

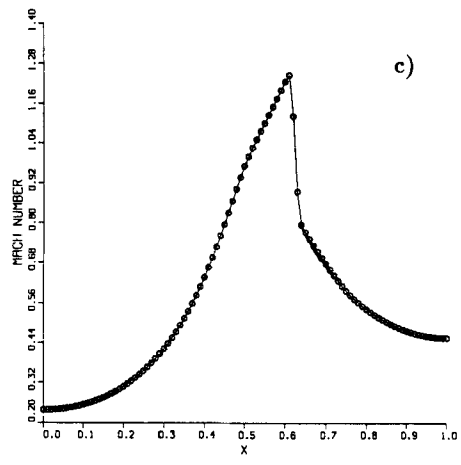

Figure 10. Unsteady quasi-1D Euler solution, $t = 1{\cdot}8$ s, $\Delta t = 0{\cdot}3$ s: ——, from Figure 6(e); (a) EU; (b) CN; (c) IRK

trapezoidal rule solution displays a crisper shock in the vicinity of the upstream curve and the shock Mach numbers are accurate. However, the downstream curve adjacent to the shock is somewhat diffused and affected by outlet oscillations. In distinction, the IRK solution remains notably superior, with very little distortion downstream of a visibly crisp shock, which has been computed at the maximum Courant number CFL = 35. Therefore these results firmly indicate that the IRK algorithm is of superior accuracy and highly competitive for this problem statement.

9.2. Two-dimensional transonic aerodynamics solutions

9.2.1. Inviscid flow. The two-dimensional Euler test investigates a transonic flow around a parabolic arc aerofoil in a channel.[24] The aerofoil thickness, based on the chord length, is 20%. The channel is three chords long and one chord wide. The modestly non-uniform grid contains 65×35 bilinear finite elements, yielding 2376 nodes, and is body-fitted with vertical lines remaining parallel to the y-axis (Figure 11), with mesh clustering near the aerofoil surface. Dirichlet constraints on ρ, m_y and e are applied at the inlet, while the exit boundary condition is that static pressure p_{out} that would yield a normal shock of prescribed strength in a strictly quasi-1D solution. The unsteady benchmark problem is the formation of a supersonic pocket with associated shock wave and allows critical evaluation of algorithm stability and accuracy.

The backwards Euler (EU), trapezoidal rule/Crank–Nicolson (CN) and stiffly stable implicit Rosenbrock–Runge–Kutta (IRK) procedures were each employed to integrate the TWS-generated ODE system (80), (81), with dissipation parameter set $\beta_q = 0{\cdot}2\,[1, 1, 1, 1]$, towards a steady state with extremum Mach number $M_s \simeq 1{\cdot}5$. The initial condition was established numerically from an isentropic subcritical state for an exit pressure ratio $p_{out}/p_\infty = 0{\cdot}72$ and for $M_\infty = 0{\cdot}675$ at the inlet. The resultant Mach number distribution is illustrated in perspective view in Figure 12(a). As is evident, the shock is not yet quite formed and the ENO nature of the finite element solution is clearly visible, both at the aerofoil leading and trailing edge singularities and at the outflow boundary. The decreased pressure ratio $p_{out}/p_\infty = 0{\cdot}62$ was then imposed upon this reference state to start the unsteady evolution test.

Figures 12(b)–12(d) show the resulting Mach number distribution at time $t - t_0 = 7{\cdot}9$ s as obtained using $\Delta t = 0{\cdot}1$ s with each of the three time algorithms. The CN solution has incurred a fatal instability, as evidenced by the unbounded dispersive error corrupting the solution at the aerofoil trailing edge singularity. Conversely, the EU and IRK solutions are ENO and appear virtually identical with $M_s = 1{\cdot}13$. Note that the Mach contour lines intersect the far-field boundary orthogonally, indicating an accurate boundary condition enforcement.

Since the CN solution subsequently diverges, the conclusion is that the upper limit on the CN stable time step is smaller than that for the EU or IRK algorithms for this problem. Therefore the

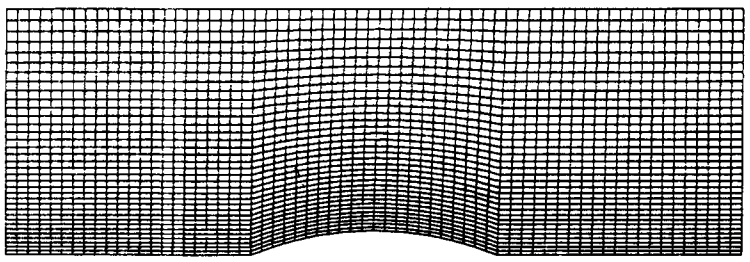

Figure 11. $M = 65 \times 35$ non-uniform mesh for transonic parabolic arc problem

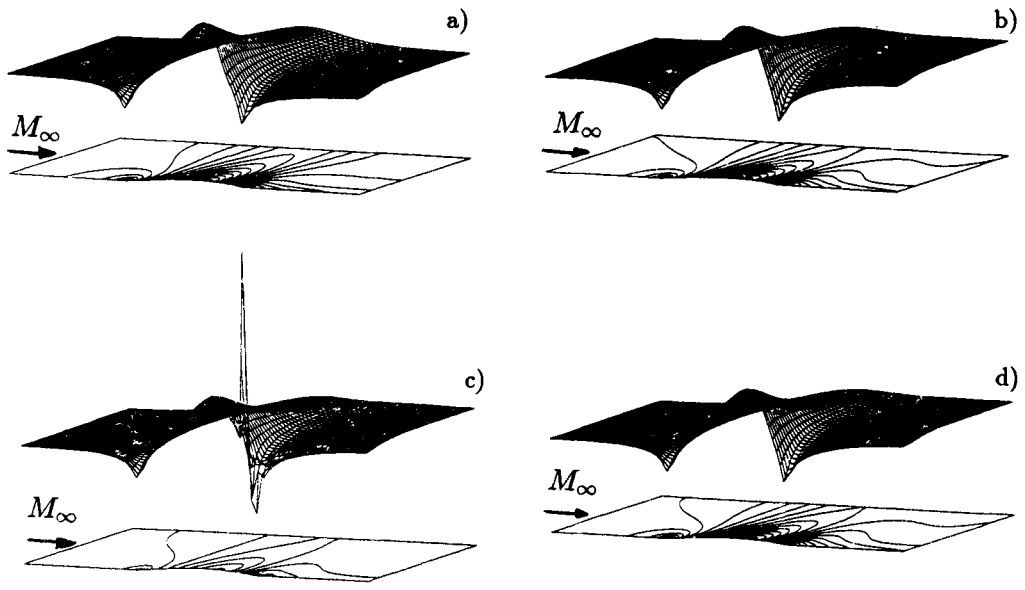

Figure 12. TWS algorithm unsteady solution, Euler equations, $t-t_0=2{\cdot}0$ s, transonic Mach number surface perspective and contours: (a) initial state; b) backwards Euler algorithm ($\theta=1$); (c) trapezoidal rule ($\theta=\frac{1}{2}$); (d) implicit Runge–Kutta algorithm

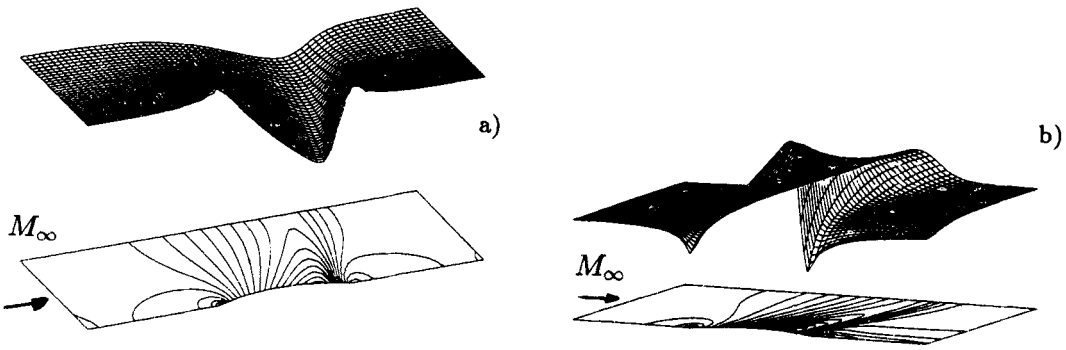

Figure 13. TWS algorithm unsteady solution perspective and contours, Euler equations, $t-t_0=14{\cdot}65$ s, $\Delta t=0{\cdot}15$ s, backwards Euler integration rule: (a) pressure; (b) Mach number

comparison continued with only the last two procedures. Now setting $\Delta t=0{\cdot}15$ s, Figures 13(a) and 14(a) compare the static pressure distributions at time $t-t_0=14{\cdot}65$ s, while Figures 13(b) and 14(b) illustrate the relevant solution Mach number distributions. Both pressure surfaces clearly show peaks at the aerofoil leading and trailing edge singularities, which are preceded by a one-cell undershoot. (Presumably, this could be eliminated with an appropriate local grid refinement.) Away from these regions the pressure surfaces are ENO along the forming shock, which extends over three elements, and everywhere along the far-field and outflow boundaries.

The associated contour plots of pressure indicate an emerging qualitative difference between these two TWS solutions. This can also be seen in the Mach number distributions, which display a crisper shock, hence better accuracy, for the IRK procedure. The EU Mach number curve along

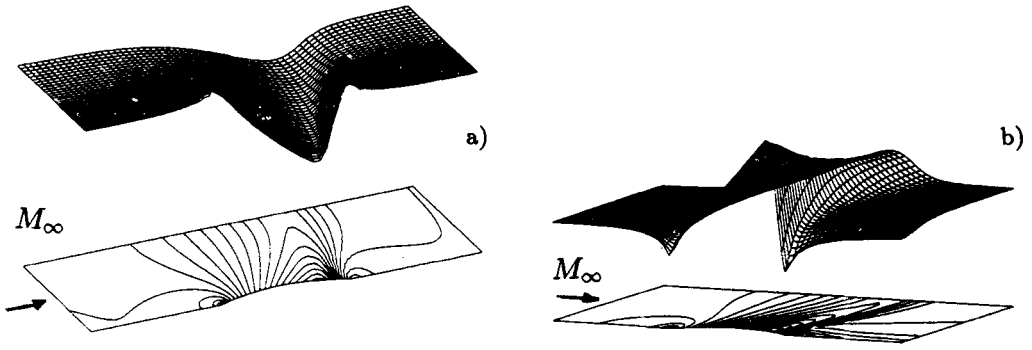

Figure 14. TWS algorithm unsteady solution perspective and contours, Euler equations, $t-t_0=14{\cdot}65$ s, $\Delta t=0{\cdot}15$ s, implicit Runge–Kutta algorithm: (a) pressure; (b) Mach number

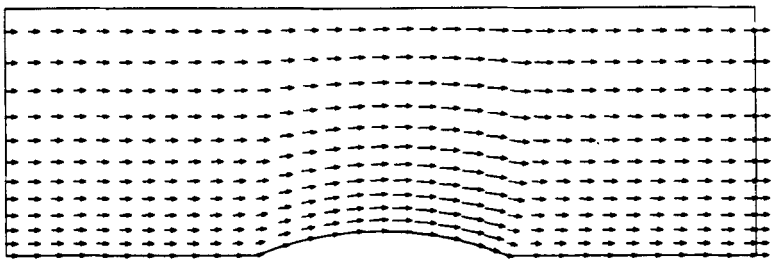

Figure 15. TWS algorithm steady state velocity vector field, Euler equations, parabolic arc, $M_s \simeq 1{\cdot}5$

the aerofoil appears somewhat rounded two cells before the shock. Moreover, the peak Mach number ($M_s=1{\cdot}401$) is not attained on the aerofoil surface but instead lies on the adjacent streamwise grid line. Conversely, the IRK solution aerofoil Mach number curve bends sharply to negotiate the shock; further, the Mach number monotonically decreases from $M_s=1{\cdot}46$ into the field.

Continued use of the fixed $\Delta t=0{\cdot}15$ s caused the EU procedure to slowly diverge as the solution continued beyond this time level. Conversely, the IRK procedure converged directly to a steady state at the maximum Courant number $C_{max}=100$. Hence the IRK algorithm admits the largest stable time step among the procedures investigated for this benchmark problem. The final steady state solution is documented in Figures 15–18. Figure 15 shows the velocity field; note that the shock is very close to the aerofoil trailing edge singularity. Figure 16 presents the contour plots of entropy, Mach number and the x-component of momentum. The entropy contours illustrate the production of entropy along the shock front. They also indicate that the TWS algorithm has generated a modest increase in entropy starting from the leading edge. Here again, this leading-edge-singularity-induced error can be eliminated with a local grid refinement. The contours of the x-component of momentum are ENO and contain virtually parallel segments orthogonally aligned along the shock. This pattern represents the nominal momentum Rankine–Hugoniot jump condition approximation, also readily evident in Figure 6(a) for the de Laval nozzle test.

A further assessment of TWS solution quality is presented in Figure 17, which contains the surface perspective representation and contour plots of each component of the momentum

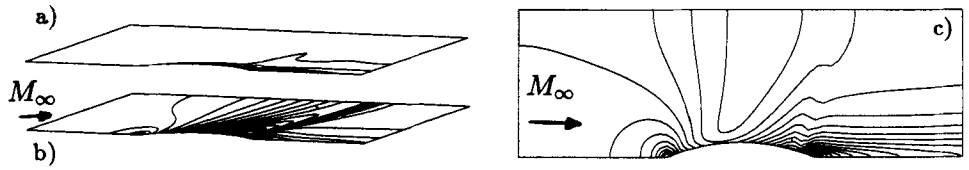

Figure 16. TWS algorithm steady state solution contours, Euler equations, parabolic arc, $M_s \simeq 1{\cdot}5$: (a) entropy; (b) Mach number; (c) principal momentum

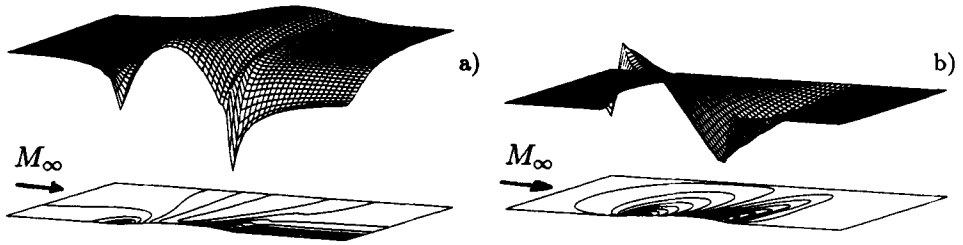

Figure 17. TWS algorithm steady state solution surface and contours: (a) principal momentum; (b) transverse momentum

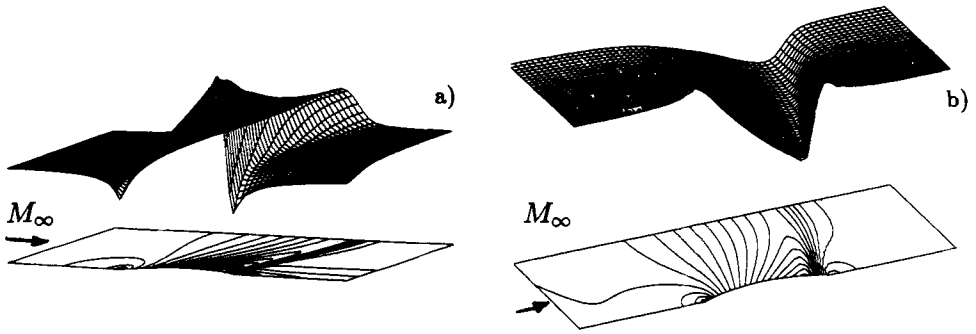

Figure 18. TWS algorithm steady state solution surface and contours: (a) Mach number; (b) pressure

vector. In both surfaces a one-cell-wide transverse plateau in the mesh emanates from the aerofoil and propagates upwards along the shock front. The local gradients in the surface of the principal momentum are quite substantial, especially at the leading and trailing edges, yet these singularities are negotiated without apparent under- or overshoot. Note how the outflow principal momentum distribution remains planar from the upper wall to about mid-channel, at the upstream state, and then smoothly decreases towards the lower boundary as total pressure is lost. The regularity of this curve also reflects favourably on the outflow pressure boundary condition enforcement. Finally, Figure 18 shows the steady state static pressure and Mach number distributions. Again, the contour lines intersect the upper wall orthogonally. The pressure surface appears ENO everywhere, with the possible exception of the leading and trailing edges singularities. The Mach number distribution also exhibits this feature, and the shock is quite crisp and captured within three elements with $M_s = 1{\cdot}528$.

9.2.2. Viscous flow. The two-dimensional Navier–Stokes tests are two viscous flows at different Reynolds numbers, both based on the aerofoil chord, in the channel geometry of the previous inviscid problem. The first test corresponds to $Re \approx 2000$ and the second to the increased value $Re = 4 \times 10^6$, more representative of practical aerodynamics applications. The relevant mesh for the first simulation, Figure 19(a), still contains $M = 65 \times 35$ elements. However, the rather non-uniform element distribution now clusters more nodes at the aerodynamic surface where $\Delta y_{\min} = 0{\cdot}02$. This mesh has permitted numerical simulations characterized by satisfactory compressible boundary layer resolution for this Reynolds number. The principal validation sought is adequacy of the derived viscous flow boundary condition specifications; whereupon, the developed steady state can be used as convenient initial flow field initialization for the larger-Reynolds-number case.

The inlet condition corresponds to $M_\infty = 0{\cdot}615$ and Dirichlet constraints on ρ, m_y and e are specified along with vanishing normal deviatoric traction. The various slip wall specifications are vanishing transverse momentum and tangential tractions. The aerofoil surface constraints are vanishing momentum vector and heat flux. Finally, the exit boundary conditions are specified as p_{out} along with vanishing deviatoric tractions and heat flux.

The $Re = 2000$ steady state solution predicts a maximum Mach number $M_{\max} = 0{\cdot}95$ and is summarized in Figures 19–21. Figures 19(b) and 19(c) graph the Mach number perspective surface and velocity vector field respectively as obtained for $\beta_q = 0{\cdot}2[1, 1, 1, 1]$. The laminar boundary layer appears to be satisfactorily resolved except perhaps for the significant leading edge stagnation region gradients. The Mach number surface terminates with a negative transverse slope at the trailing edge, which signals separation and an emerging recirculation zone. This is confirmed in the velocity vector field close-up detail, Figure 20(a). The Mach number isocline distribution, Figure 20(b), illustrates this important flow characteristic along with the merging of the essentially inviscid outer flow with the boundary layer and viscous wake.

The latter is further illustrated in Figure 21, which graphs distributions of both components of the momentum vector as well as static pressure and temperature. The surface perspective

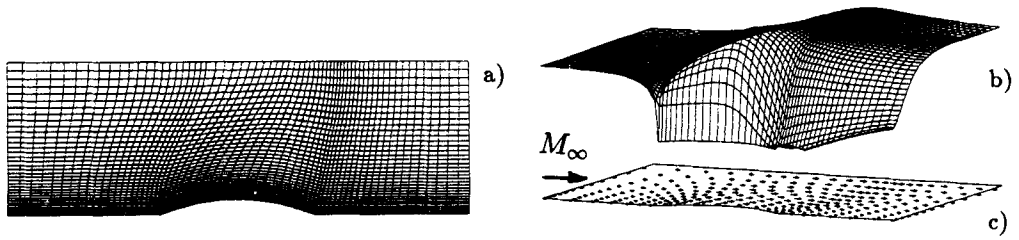

Figure 19. TWS algorithm steady state solution, Navier–Stokes equations, laminar $Re = 2000$: (a) $M = 65 \times 35$ element discretization; (b) Mach number distribution; (c) velocity vector field

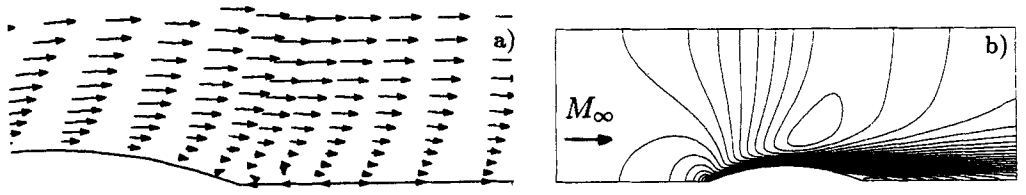

Figure 20. TWS algorithm steady state solution, Navier–Stokes equations, laminar $Re = 2000$: (a) trailing edge region velocity vector field; (b) Mach number isocline distribution

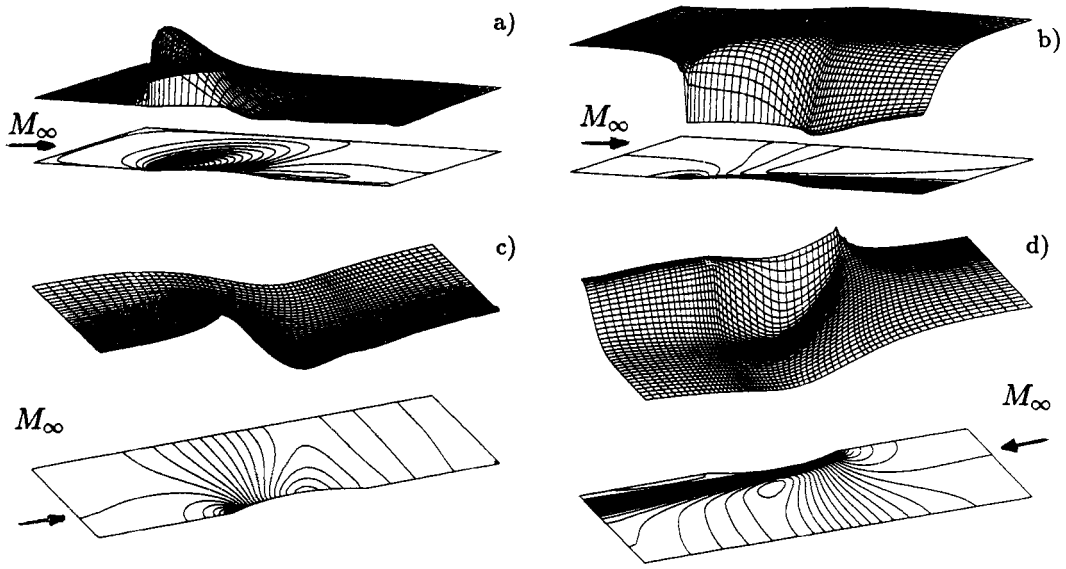

Figure 21. TWS algorithm steady state solution, Navier–Stokes equations, laminar $Re = 2000$: (a) transverse momentum; (b) principal momentum; (c) pressure; (d) temperature

presentations clearly emphasize the flow detail, including the leading edge stagnation point peak, accompanied by a modest one-cell undershoot. Hence $Re = 2000$ is indeed the maximum this grid can support. Note how the outflow principal momentum distribution remains planar from the upper wall to about mid-channel and then smoothly declines towards the lower boundary value. This character is accompanied by a decisive temperature increase that initiates at the leading edge and continuously progresses towards the outlet. The regularity of all distributions reflects favourably on the viscous flow boundary condition definitions and enforcement procedure.

This solution was employed as initial state for a subsequent simulation with increased Reynolds number $Re = 4{\cdot}6 \times 10^6$ to compute a practical viscous transonic aerodynamics problem. The incipient leading edge oscillations in the results of the previous viscous problem test indicate the need for a more refined and adapted mesh. Hence the mesh for this test is now composed of $M = 65 \times 45$ bilinear elements with considerable node clustering at the trailing and leading edges as well as on the aerodynamic surface, which now corresponds to a 4% thick aerofoil, as shown in Figure 22(a). In the aerodynamic surface region the mesh has adequate wall resolution with vertical measure equal to $1/Re$; therefore the transverse physical diffusion components can support the same order of magnitude as the longitudinal convection components. The TWS stability parameter set remained fixed at $\beta_q = 0{\cdot}2[1, 1, 1, 1]$, and for the boundary conditions of the previous test, a nominal steady state was achieved in about 800 time steps at the maximum Courant number $C_{\max} = 100$. The corresponding inlet Mach number was $M_\infty = 0{\cdot}7$. At this stage the sup-norm $\| R \|_\infty$ of the normalized residual decreased to $O(10^{-5})$. It was noted that for single-precision calculations the values of this norm oscillated boundedly in the range $O(10^{-5}) \leqslant \| R \|_\infty \leqslant O(10^{-6})$. This behaviour was localized on the second half of the aerofoil, whereas $\| R \| \approx O(10^{-8})$ elsewhere on the computational domain.

Figures 22(b) and 23(a) are contour plots of axial momentum distribution in physical Cartesian space (x, y) and in the stretched transverse nodal (x, η_2) space respectively. The latter presentation clearly shows that a local shock-induced massive separation occurs just past mid-chord and

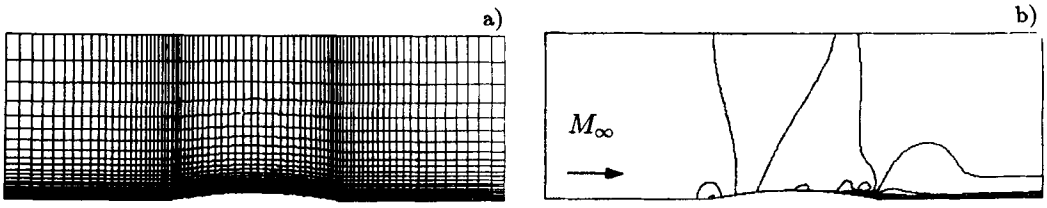

Figure 22. TWS algorithm steady state solution, Navier–Stokes equations, laminar $Re = 4 \times 10^6$: (a) $M = 65 \times 45$ element discretization; (b) physical space principal momentum contour distribution

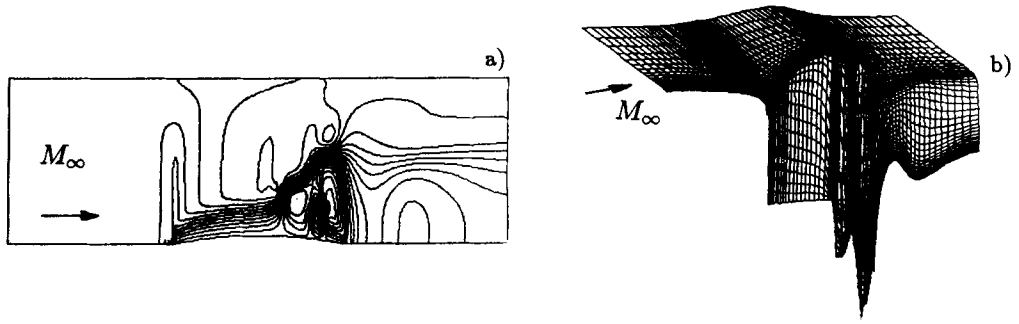

Figure 23. TWS algorithm steady state principal momentum solution, Navier–Stokes equations, laminar $Re = 4 \times 10^6$: (a) transverse nodal space contour distribution; (b) perspective surface presentation

extends to well beyond the trailing edge. This region, according to the computations, appeared marginally unsteady. Figure 23(b) graphs a perspective view of the axial momentum distribution, hence correlates with Figures 17 and 21. The solution appears virtually ENO and sufficiently resolves the essential flow features. Note that the decrease of momentum to zero at the leading edge and along the aerofoil surface occurs smoothly, with the possible exception of a modest two-cell under- or overshoot preceding the stagnation point. Note also that the outlet variation of this variable is totally devoid of dispersive oscillations. This distribution remains virtually planar in the essentially inviscid flow region and then drastically decreases in the viscous layer in a monotone way. Therefore the validity of the outlet boundary condition choice for this case, as discussed at the end of Section 4.1, is evidently supported by the regularity of this result.

The shock wave boundary layer interaction is vividly depicted in the region just past mid-chord. This consists of two recirculation zones, the second being wider than the first. This significant flow activity then subsides in a wavy pattern in the wake originating after the trailing edge. Figure 24(a) shows the associated persective distribution of static pressure, which appears ENO everywhere, particularly at the stagnation point. The main difference between these data and those in Figure 21 lies in the recirculation zone pressure variation. The latter is detailed in the close-up graph in Figure 24(b). Note that a virtual plateau exists in the primary recirculation zone; whereupon, the local shock triggers the pressure rise. Possibly the attendant boundary layer thickening in this region significantly alters the cross-sectional area distribution to the extent of producing a virtual converging channel for the outer inviscid subsonic flow, which therefore accelerates. This event seems compatible with a decrease in pressure following its rise across the shock. This low-pressure area is then terminated by a second shock and accompanying trailing edge recompression. This second pressure increase then causes the second separation, as illustrated in the momentum distribution in Figure 23(b).

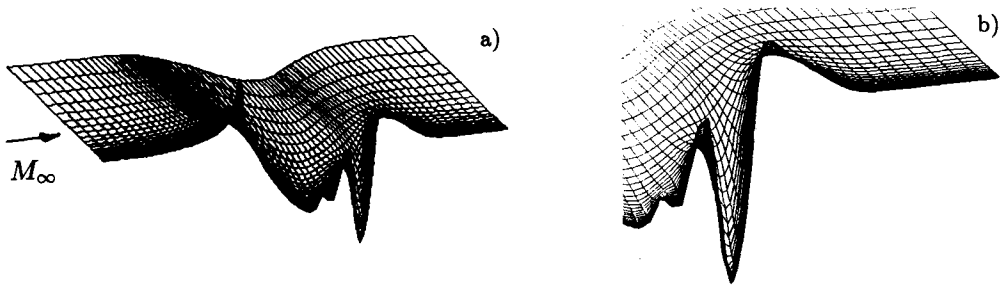

Figure 24. TWS algorithm steady state pressure solution, perspective surface presentations, Navier–Stokes equations, laminar $Re = 4 \times 10^6$: (a) global distribution; (b) trailing edge region detail

This numerical simulation has been the first practical transonic aerodynamics viscous problem computed with the derived TWS algorithm, and the results seem to conform with expected shock–boundary layer interaction phenomena. However, no experimental data are known for this challenging practical problem, hence independent solution validation is not attainable at present.

10. CONCLUSIONS

A stable and accurate finite element CFD algorithm for the laminar compressible Navier–Stokes and Euler conservation law systems is described and verified. It constitutes the union of a Taylor weak statement finite element semi-discretization, an optimal implicit Rosenbrock–Runge–Kutta integration algorithm and a matrix tensor product approximate factorization linear algebra procedure. The study is complemented by a full theoretical development of well-posed boundary conditions for all Reynolds and Mach numbers. These conditions constrain the surface deviatoric tractions and momentum and heat flux and are directly enforceable via the surface integrals exposed in weak statement constructions.

The TWS algorithm plays a central role in the achievement of stable solutions by generating a suitably dissipative semi-discrete ODE system. The amount of stability correction is regulated by the parameters β_q, which were initially determined heuristically for the selected benchmark problems. Their values have been held uniformly constant and the regularity of the documented results supports their adequacy. A complementary theory has been initiated[25] that leads to a rigorous and automatic determination of these dissipation parameters. Anyhow, the developed algorithm has uniformly maintained its robustness over a wide range of challenging inviscid and viscous flow problems, without problem-dependent 'fine tuning'. These selections are independent of mesh distribution, as especially revealed by the 2D inviscid flow results.

Concerning the viscous tests, the results are stable as well as ENO and conform to the fundamental physics of the problems investigated. With this fundamental background, the authors are progressing in the assessment of the delicate interplay between artificial dissipation and physical diffusion via examination of a well-documented laminar boundary layer–shock wave interaction problem in a supersonic flow over a flat plate. The results will be reported in a forthcoming paper.

In regards to time accuracy and swift convergence to steady state, the quasi-1D tests reveal that the IRK procedure yields uniformly more accurate and stable results than those generated by the equivalently second-order-accurate trapezoidal rule. This is probably due to a reduced IRK truncation error coefficient, as possibly promoted by the enforced stiff stability with respect to a

non-linear model problem. Further, the 2D inviscid flow tests indicate that IRK affords the largest usable Courant number. Hence this implicit Rosenbrock–Runge–Kutta algorithm constitutes an advantageous and economical alternative to the single-step procedures now in general use in CFD codes.

ACKNOWLEDGEMENTS

This research has been partially supported by NASA Ames Research Center under SBIR Phase II contract NAS2-12568 with Computational Mechanics Corporation, Knoxville, TN. The authors gratefully acknowledge the support of The University of Tennessee Computer Center, the industrial sustaining members of the UT Computational Fluid Dynamics Laboratory, and the Cornell National Supercomputer Facility.

REFERENCES

1. R. M. Beam and R. F. Warming, 'An implicit finite-difference algorithm for hyperbolic systems in conservation-law form', *J. Comput. Phys.*, **22**, 87–110 (1976).
2. T. H. Pulliam, 'Efficient solution methods for the Navier–Stokes equations', *Lecture Notes, Von Karman Institute Lecture Series, Numerical Techniques for Viscous Flow Computation in Turbomachinery Bladings*, Brussels,1986.
3. J. L. Steger and R. F. Warming, 'Flux vector splitting of the inviscid gasdynamics equations with applications to finite difference methods', *J. Comput. Phys.*, **40**, 263–293 (1981).
4. B. van Leer, 'Flux-vector splitting for the Euler equations', *Lecture Notes in Physics*, Vol. 170, Springer, Berlin, 1982, pp. 507–512.
5. P. L. Roe, 'Approximate Riemann solvers, parameter vectors, and difference schemes', *J. Comput. Phys.*, **43**, 357–372 (1981).
6. M. S. Liou and B. van Leer, 'Choice of implicit and explicit operators for the upwind differencing method', *Tech. Paper AIAA 88-0624, 26th Aerospace Sciences Meeting*, Reno, NV, 1988.
7. K. G. Powell and B. van Leer, 'A genuinely multi-dimensional upwind cell-vertex scheme for the Euler equations', *NASA Tech. Memorandum 102029 ICOMP-89-13*, 1989.
8. A. Lerat, 'Implicit methods of second-order accuracy for the Euler equations', *Tech. Paper AIAA 83-1925, 6th Computational Fluid Dynamics Conf.*, 1983.
9. C. A. Fletcher, *Computational Galerkin Methods*, Springer, New York, NY, 1984.
10. T. E. Tezduyar and T. J. R. Hughes, 'Finite element formulations for convection dominated flows with particular emphasis on the compressible Euler equations', *Tech. Paper AIAA 83-0125, 21st Aerospace Sciences Meeting*, Reno, NV, 1983.
11. J. Donea, 'A Taylor–Galerkin method for convective transport problems', *Int. j. numer. methods eng.*, **20**, 101–119 (1984).
12. A. J. Baker and J. W. Kim, 'A Taylor weak statement algorithm for hyperbolic conservation laws', *Int. j. numer. methods fluids*, **7**, 489–520 (1987).
13. P. Dutt, 'Stable boundary conditions and difference schemes for Navier–Stokes equations', *SIAM J. Numer. Anal.*, **25**, 245–267 (1988).
14. V. I. Zubov, *Methods of A. M. Lyapunov and their Application*, U.S. Atomic Energy Commission AEC-52-4439, Office of Technical Services, Department of Commerce, Washington, DC, 1961.
15. W. Hahn, *Theory and Application of Lyapunov's Direct Method*, Prentice-Hall, Englewood Cliffs, NJ, 1963.
16. T. Yoshizawa, *Stability Theory by Lyapunov's Second Method*, The Mathematical Society of Japan, Gakujutsutosho Co., Ltd. Tokyo, Japan, 1966.
17. G. S. Iannelli and A. J. Baker, 'A stiffly-stable implicit Runge–Kutta algorithm for CFD applications', *Tech. Paper AIAA 88-0115, 26th Aerospace Sciences Meeting*, Reno, NV, 1988.
18. N. Coburn, *Vector and Tensor Analysis*, Macmillian, New York, NY, 1955.
19. A. J. Baker, *Finite Element Computational Fluid Mechanics*, Hemisphere, Washington, DC, 1983.
20. J. C. Strickwerda, 'Initial boundary value problems for incompletely parabolic systems', *Commun. Pure Appl. Math.*, **30**, 797–822 (1977).
21. L. J. Hayes, 'Implementation of finite element alternating direction methods on non-rectangular regions', *Int. j. numer. methods eng.*, **16**, 35–49 (1980).
22. L. J. Hayes, 'Galerkin alternating-direction methods for non-rectangular regions using patch approximations', *SIAM J. Numer. Anal.*, **18**, 627–643 (1981).
23. M. A. Celia and G. F. Pinder, 'An analysis of alternating direction methods for parabolic equations', *Numer. Methods Partial Diff. Eqn.*, **1**, 57–70 (1985).
24. G. M. Johnson, 'Relaxation solution of the full Euler equations', *Lecture Notes in Physics*, Vol. 170, Springer, Berlin, 1982, pp. 273–279.

25. G. S. Iannelli and A. J. Baker, 'Towards a rational theory for CFD global stability', *Tech. Paper AIAA 89-1988, 9th Computational Fluid Dynamics Conf.*, Buffalo, NY, 1989.
26. J. D. Lambert, *Computational Methods in Ordinary Differential Equations*, Wiley, New York, NY, 1973.
27. V. Hutson and J. S. Pym, *Applications of Functional Analysis and Operator Theory*, Academic Press, New York, NY, 1980.
28. K. Dekker and J. G. Verwer, *Stability of Runge–Kutta Methods for Stiff Nonlinear Differential Equations*, Elsevier, New York, NY, 1984.
29. J. C. Butcher, *The Numerical Analysis of Ordinary Differential Equations: Runge–Kutta and General Linear Methods*, Wiley, New York, NY, 1987.
30. B. van Leer, 'Towards the ultimate conservative difference scheme, II Monotonicity and conservation combined in a second order scheme', *J. Comput. Phys.*, **14**, 361–370 (1974).
31. K. Burrage and J. C. Butcher, 'Stability criteria for implicit Runge–Kutta methods', *SIAM J. Numer. Anal.*, **16**, 46–57 (1979).
32. W. H. Hundsdorfer and M. N. Spijker, 'A note on B-stability of Runge–Kutta methods', *Numer. Math.*, **36**, 319–331 (1981).
33. P. Kaps and G. Wanner, 'A study of Rosenbrock-type methods of high order', *Numer. Math.*, **38**, 297–298 (1981).
34. G. S. Iannelli and A. J. Baker, 'An implicit and stiffly stable finite element CFD algorithm for aerodynamic applications', *Tech. Paper AIAA-89-0656, 27th Aerospace Sciences Meeting*, Reno, NV, 1989.